Atmos. Chem. Phys. Discuss., 14, 24753–24810, 2014
www.atmos-chem-phys-discuss.net/14/24753/2014/
doi:10.5194/acpd-14-24753-2014

Atmospheric Chemistry and Physics Discussions

Molecular characterization of free tropospheric aerosol collected at the Pico Mountain Observatory: a case study with long range transported biomass burning plumes

K. Dzepina[1,2], C. Mazzoleni[2,3], P. Fialho[4], S. China[2,3], B. Zhang[2,5], R. C. Owen[2,*], D. Helmig[6], J. Hueber[6], S. Kumar[2,3,], J. A. Perlinger[5], L. Kramer[2,7], M. P. Dziobak[7], M. T. Ampadu[1], S. Olsen[8,***], D. J. Wuebbles[8], and L. R. Mazzoleni[1,2,7]**

[1]Department of Chemistry, Michigan Technological University, Houghton, MI, USA
[2]Atmospheric Science Program, Michigan Technological University, Houghton, MI, USA
[3]Department of Physics, Michigan Technological University, Houghton, MI, USA
[4]Department of Agricultural Sciences, University of the Azores, Angra do Heroísmo, Portugal
[5]Department of Civil and Environmental Engineering, Michigan Technological University, Houghton, MI, USA
[6]Institute of Arctic and Alpine Research (INSTAAR), University of Colorado, Boulder, CO, USA

[7]Department of Geological and Mining Engineering and Sciences, Michigan Technological University, Houghton, MI, USA
[8]Department of Atmospheric Science, University of Illinois, Urbana Champaign, IL, USA
[*]now at: US EPA, Research Triangle Park, North Carolina, USA
[**]now at: National Center for Medium Range Weather Forecasting, Noida, India
[***]now at: Xyratex International Ltd, Sacramento, CA, USA

Received: 15 August 2014 – Accepted: 23 August 2014 – Published: 25 September 2014

Correspondence to: K. Dzepina (kdzepina@mtu.edu)
and L. R. Mazzoleni (lrmazzol@mtu.edu)

Published by Copernicus Publications on behalf of the European Geosciences Union.

ACPD
14, 24753–24810, 2014

Abstract

Free tropospheric aerosol was sampled at the Pico Mountain Observatory located at 2225 m a.m.s.l. on Pico Island of the Azores archipelago in the North Atlantic. The observatory (38°28′15″ N; 28°24′14″ W) is located ∼ 3900 km east and downwind of North America, which enables studies of free tropospheric air transported over long distances, mainly from North America. Aerosol samples collected on filters from June to October 2012 were analyzed to characterize organic carbon, elemental carbon and inorganic ion species. The average ambient concentration of aerosol was 0.9 µg m^{-3}; on average organic aerosol contributes the majority of mass (57 %), followed by sulfate (21 %) and nitrate (17 %). Filter-collected aerosol measurements were positively correlated (with an $r^2 \geq 0.80$) with continuous aerosol measurements of black carbon, aerosol light scattering and number concentration. Water-soluble organic carbon (WSOC) species extracted from two aerosol samples (9/24 and 9/25) collected consecutively during a pollution event were analyzed using ultrahigh-resolution Fourier transform ion cyclotron resonance mass spectrometry. FLEXPART retroplume analysis shows the sampled air masses were very aged (average plume age > 12 days). Approximately 4000 molecular formulas were assigned to each of the mass spectra in the range of m/z 100–1000. The majority of the assigned molecular formulas have unsaturated structures with CHO and CHNO elemental compositions. These aged WSOC compounds have an average O/C ratio of ∼ 0.45, which is relatively low compared to O/C ratios of other aged aerosol and might be the result of evaporation and increased fragmentation during long-range transport. The increase in aerosol loading during the measurement period of 9/24 was linked to biomass burning emissions from North America by FLEXPART retroplume analysis and Moderate Resolution Imaging Spectroradiometer (MODIS) fire counts. This was confirmed with biomass burning markers detected in WSOC species and with the morphology and mixing state of particles as determined by scanning electron microscopy. The presence of markers characteristic of aqueous-phase reactions of biomass burning phenolic species suggests that the

ACPD
14, 24753–24810, 2014

aerosol collected at the Pico Mountain Observatory had undergone cloud processing before reaching the site. Finally, the air masses on 9/25 were more aged (~ 15 days) and influenced by marine emissions, as indicated by organosulfates and other species characteristic for marine aerosol such as fatty acids. The change in air masses for the two samples was corroborated by the changes in ozone and the non-methane hydrocarbons ethane and propane, morphology of particles, as well as by the FLEXPART retroplume simulations. This manuscript presents the first detailed molecular characterization of free tropospheric aged aerosol intercepted at a lower free troposphere remote location in the North Atlantic.

1 Introduction

The low scientific understanding in the properties and transformations of atmospheric aerosol is the key uncertainty in determining the anthropogenic climate forcing through its direct, semi-direct and indirect radiative effects (IPCC, 2013). Organic aerosol (OA) can comprise 20–90 % of atmospheric aerosol mass (Kanakidou et al., 2005; Zhang et al., 2007), and are the least understood component of aerosol. Atmospheric OA include both primary and secondary OA (POA and SOA, respectively). POA are emitted directly into the atmosphere, while SOA are produced by homogeneous nucleation, oxidative reactions of gaseous organic precursors and condensation of their products onto pre-existing particles, and aqueous phase reactions in cloud, fog and particulate water (Hallquist et al., 2009). The properties of aerosol in regions downwind of emission sources are impacted by the outflow of pollutants, their chemical transformation, and sinks. In particular, remote locations can be dominated by SOA (Zhang et al., 2007). Ambient water-soluble organic carbon (WSOC) compounds are estimated to account for up to 80 % of OA mass (Saxena, 1996; Sun et al., 2011), but these species are still not well characterized on a molecular level (Reemtsma, 2009). A significant fraction of the WSOC is comprised of higher molecular weight humic-like substances (HULIS) (Graber and Rudich, 2006) and biogenic SOA (Schmitt-Kopplin et al., 2010; Mazzoleni

ACPD
14, 24753–24810, 2014

et al., 2012). The identification of WSOC composition is challenging. There are thousands of species present as WSOC that have a wide range of elemental compositions and molecular weights, with multiple functional groups such as carboxyl, hydroxyl, carbonyl, nitro, nitrate, and sulfate. Molecular characterization of WSOC is important for understanding its roles in fundamental processes such as impacts on optical properties such as light absorption and scattering (Dinar et al., 2006; Shapiro et al., 2009; Nguyen et al., 2013), chemical reduction/oxidation mediation (Kundu et al., 2012), and aerosol water uptake and reactivity (Ervens and Volkamer, 2010; Ervens et al., 2011). Aqueous SOA formation in clouds might explain the current model under-predictions of OA concentrations, especially at high altitudes (Carlton et al., 2008). Determination of the OA molecular composition is a challenging task. Theoretical calculations indicate the possibility of millions of OA chemical species (Goldstein and Galbally, 2007; Aumont et al., 2005), although recent research reports a more uniform composition of OA, which suggests a far smaller number of compounds (Jimenez et al., 2009; Kroll et al., 2011; Laskin et al., 2012; Mazzoleni et al., 2012). Analytical methods capable of characterizing OA at the molecular level are necessary to tackle this problem.

In the last few decades, instruments based on mass spectrometry have become the gold standard for OA measurements (Canagaratna et al., 2007; Pratt and Prather, 2012a, b; Laskin et al., 2012). The most important characteristics of a mass spectrometer for the analysis of complex mixtures such as ambient OA are its mass resolution and accuracy (Lobodin et al., 2012). The mass spectrometer with the highest mass resolution and accuracy is the Fourier Transform Ion Cyclotron Resonance Mass Spectrometer (FT-ICR MS; He et al., 2001). In the FT-ICR MS instrument, excited ions induce an ion current proportional to their exact mass that is detected as a frequency vs. time spectrum, and with the use of FT this spectrum is converted to intensity vs. m/z. Typically FT-ICR MS mass resolving power and accuracy used for analysis of ambient aerosol are 200 000–400 000 and < 2 ppm, respectively (Mazzoleni et al., 2010). When combined with an appropriate ionization technique, FT-ICR MS is capable of resolving thousands of chemically different species in a single mass spectrum, and is

ACPD
14, 24753–24810, 2014

ideally suited for the analysis of complex mixtures of ambient OA. Electrospray ionization (ESI) is a soft ionization technique that leaves the sample molecules intact and minimizes their fragmentation, and thus is ideal for coupling with FT-ICR MS for detailed molecular level characterization of OA (Nizkorodov et al., 2011). ESI ionizes polar molecules and when operated in the "negative mode", ions are formed in solution by deprotonation and thus are negatively charged. Negative ESI is especially useful for the ionization of multifunctional oxidized compounds such as carboxylic and dicarboxylic acids. FT-ICR MS was successfully used for the analysis of ambient OA (Wozniak et al., 2008; Schmitt-Kopplin et al., 2010; Mazzoleni et al., 2012) and dissolved organic matter (OM) in rain (Altieri et al., 2009a, 2009b, 2012; Mead et al., 2013; Zhao et al., 2013), fog water (Mazzoleni et al., 2010), and sea spray aerosol (Schmitt-Kopplin et al., 2012).

The long-range transport of aerosol from Asia to North America has received considerable attention (Ramanathan et al., 2007; Dunlea et al., 2009), but less attention has been placed on aerosol transported from North America to Europe. The Pico Mountain Observatory (PMO) is an ideal site for observations of free tropospheric air masses and pollutants from North America after trans-Atlantic transport (Val Martin et al., 2006, 2008a). The observatory is located at 2225 m a.m.s.l. in the summit caldera of a dormant volcano on Pico Island in the Azores archipelago in the North Atlantic (Supplement Fig. S1). The observatory is typically above the marine boundary layer height of 850–1100 m a.m.s.l. during summer (Kleissl et al., 2007), and is rarely affected by local emissions. Deeper marine boundary conditions with heights up to 1700 m a.m.s.l. have been reported for colder months (Kleissl et al., 2007) and of about 1500 m a.m.s.l. for the other islands of the Azores archipelago (Remillar et al., 2012), although it always remains lower than the altitude of PMO. The measurements at the PMO began in July 2001 with a focus on gaseous species, black carbon and meteorological parameters. Previous measurements at PMO and dispersion model simulations indicated that outflow of North American tropospheric ozone and its precursors are frequently encountered at PMO. These results were crucial in explaining the evolution of

ACPD
14, 24753–24810, 2014

North American gaseous pollution and identified the significant impact of CO, O_3, NO_x and NO_y from boreal biomass burning pollution on background air composition over the North Atlantic (Honrath et al., 2004; Lapina et al., 2006; Val Martin et al., 2006; Owen et al., 2006; Pfister et al., 2006), and enhanced understanding of the oxidation of non-methane hydrocarbons (NMHC) (Helmig et al., 2008; Honrath et al., 2008). Fialho et al. (2005, 2006) developed a method to determine the contribution of black carbon (BC) and dust from the aethelometer measurements. Although typically average free tropospheric aerosol concentrations are relatively low, long-range transport events bring in BC and dust mass concentrations at elevated levels. A recent analysis of peroxycarboxylic nitric anhydrides (PANs) measured at the PMO showed that they are transported to the observatory during colder, spring months, but not in warmer summer months due to their thermal instability (K. Dzepina, J. Roberts and the Pico Mountain Observatory team, personal communication, 2014), consistent with previous estimates (Val Martin et al., 2008b).

This paper reports the first detailed chemical characterization of tropospheric aged aerosol sampled at the PMO during the summer of 2012. Detailed analysis of WSOC molecular composition results from ultrahigh resolution FT-ICR MS measurements was performed for two aerosol samples collected during 24–26 September when a pollution event with the highest loading of fine particles was observed. Molecular composition of WSOC, on-line measurements, and laboratory analysis of aerosol are used together with the simulations of particle dispersion model and satellite data to deduce the emission sources and transformational processes of the fine particles sampled at the PMO.

2 Measurements and methods

2.1 Aerosol measurements at the Pico Mountain Observatory

New aerosol instrumentation was installed at PMO in 2012, including a 2-channel optical particle counter (MetOne GT-521, Grants Pass, OR, USA; in this paper, we report

ACPD
14, 24753–24810, 2014

aerosol number concentration for channel 1 with particle size range of 0.3–5 µm), a nephelometer (EcoTech Aurora 3000, Warren, RI, USA) to measure aerosol light scattering and backscattering fraction at three wavelengths (450, 525 and 635 nm), an aerosol sample collector (custom-made at Michigan Tech) for scanning and transmission electron microscopy analysis, and four high-volume air samplers (Hi-Vols; EcoTech HiVol 3000, Warren, RI, USA). The four Hi-Vols were installed in close proximity (~ 50 m) to the PMO, and they were used to collect samples from June through October 2012. They were operated at an average volumetric flow rate of 84 $m^3\,h^{-1}$ for 24 h collection of $PM_{2.5}$ (particulate matter with aerodynamic diameters ≤ 2.5 µm). High-volume cascade impactors (Tisch Environmental, TE-231 single stage High Volume Cascade Impactor, Cleves, OH, USA) were used for size selection. $PM_{2.5}$ was collected on quartz filters (Whatman, 20.3 cm × 25.4 cm Quartz Microfibre Filters, CAT No. 1851–865, Cleves, OH, USA), and particles > $PM_{2.5}$ were captured on a separate filter (Tisch Environmental, 14.3 cm × 13.7 cm Quartz Filters, Part No. TE-230 QZ, Cleves, OH, USA); the results reported here refer only to the $PM_{2.5}$ samples. Quartz filters were wrapped in aluminum foil, baked for 12 h at 550 °C, then inserted into antistatic bags (Uline 22.9 cm × 30.5 cm Reclosable Static Shielding Bags Pleasant Prairie, WI, USA) and stored at room temperature until use. Typically, filters were inserted in all four Hi-Vols during one visit to the site, and the Hi-Vols were programmed to sample consecutively for 24 h each. We should note that the site is reachable via a strenuous hike on rugged terrain (Honrath et al., 2004). Sampled filters were refrigerated locally until cold transport to the US where they were kept in a freezer until further analysis. A total of 36 filters were collected in 2012, but only 18 were selected for further laboratory analysis (Table 1) since the remaining 18 filter samples were wet from cloud and precipitation events. Due to the wet periods, we were unable to collect suitable field blanks during the 2012 campaign. Thus, a laboratory blank was used to evaluate artifacts associated with quartz filters. All measurement times reported in this manuscript are given in local time which is the same as UTC.

ACPD
14, 24753–24810, 2014

A seven wavelength aethalometer (Magee Scientific, model AE31, λ = 370, 470, 520, 590, 660, 880 and 950 nm) equipped with a "high sensitivity" circular spot size chamber was used to measure the aerosol attenuation coefficient. Ambient air was sampled at a flow rate of 7.7 $dm^3\,min^{-1}$ through a whole air inlet without size cut-off. Particulate matter accumulated on a quartz fibre filter tape (Q250F from Pallflex©). The instrument was setup to automatically advance the tape every 24 h with a measurement interval of 5 min.

Quartz filter samples from 9/24 and 9/25 were further investigated for morphological analysis using electron microscopy. Four small portions (5 mm × 5 mm) were used from different areas of each filter to obtain a representative sample. The samples were mounted on aluminum stubs and coated with a 1.8 nm thick platinum layer using a Sputter coater (Hummer 6.2). The coated filters were imaged using a Hitachi S-4700 field emission scanning electron microscope (FE-SEM). Elemental compositions of individual particles were investigated using Energy Dispersive X-Ray spectroscopy (EDS).

2.2 Measurement of OC, EC and inorganic ions

Aerosol samples were analyzed for organic and elemental carbon (OC and EC, respectively) and the reported results are an average of at least three measurements. OC and EC content was determined with an OC : EC analyzer (Sunset Laboratory Inc., Model 4, Tigard, OR, USA), which uses the thermo-optical transmittance method (Birch and Cary, 1996). OC and EC measurements were also performed for the blanks and the corresponding result was subtracted from the aerosol sample result. The blank OC values were 13 % (SD = 8 %) of average measured ambient OC mass. The blank EC values were below the detection limit and thus no EC blank subtraction was done.

Samples were also analyzed for inorganic (NO_3^-, SO_4^{2-}, Cl^-, NO_2^-, Br^-, F^-, and PO_4^{3-}) and organic anions (acetate, propionate, oxalate and formate) with ion chromatography (ICS-2000 ion chromatograph with an IonPac AS11 separator column, Dionex Corporation, Bannockburn, IL, USA). Samples were prepared for anion analysis

ACPD
14, 24753–24810, 2014

by placing seven punches of 1.7 cm diameter into 12 mL of nanopure water and sonicating them twice for 30 min (total of 60 min) at room temperature. Reported results are an average of two measurements. NO_3^-, SO_4^{2-} and Cl^- only were present at concentrations above the detection limit. Results reported here have been laboratory blank subtracted for Cl^- only; Cl^- in the laboratory filter blank was 48 % (SD = 21 %) of Cl^- found in aerosol samples. Blank measurements for NO_3^- and SO_4^{2-} were below the detection limit.

2.3 Ultrahigh-resolution ESI FT-ICR MS analysis of WSOC

2.3.1 Aerosol sample preparation

The preparation of aerosol samples for FT-ICR MS analysis was done using Strata-X (Phenomenex,Torrance, CA, USA) reversed-phase solid-phase extraction (SPE) to concentrate the analytes and remove inorganic ions (Mazzoleni et al., 2010, 2012; Zhao et al., 2013). All solvents used to prepare samples for ESI FT-ICR MS analysis were of HPLC grade purity or higher. Strata-X SPE cartridges were conditioned with an application of three solvents in the following order: 3 mL of methanol, 3 mL of acetonitrile and 3 mL of optima grade HPLC water. Exactly half of 9/24 and 9/25 filters and a laboratory filter blank were cut into smaller pieces and sonicated for 30 min twice, first time in 30 mL and second time in 20 mL water. The pH was not adjusted. The 50 mL aqueous extracts were applied at a slow rate (approx. 1 mL min^{-1}) to enable aerosol organic species to partition to the SPE stationary phase. SPE cartridges were rinsed with water and the WSOC species retained on the SPE stationary phase were eluted with a 2 mL solution composed of water and acetonitrile in a 1 : 9 ratio. Prepared extracts were stored in a freezer until cold overnight shipment on freezer packs to the Woods Hole Oceanographic Institute Fourier Transform Mass Spectrometry facility for analysis.

ACPD
14, 24753–24810, 2014

2.3.2 ESI FT-ICR MS instrumental parameters

Aerosol WSOC samples and blanks were analyzed at the Woods Hole Oceanographic Institute Fourier Transform Mass Spectrometry facility using the ultrahigh-resolution 7 tesla FT-ICR mass spectrometer (LTQ FT Ultra, Thermo Scientific, San Jose, CA) equipped with an ESI source. Samples were infused directly into the ESI interface and the ESI parameters were adjusted to obtain a stable ion current with minimum ion injection time into the mass analyzer. After optimization, the infusion flow rate was 4 µL min^{-1} and the ESI needle voltage was −3.9 kV. Between measurements, the sample delivery apparatus was flushed with at least 500 µL of pure water and acetonitrile and their solution in 1 : 9 ratio until background noise levels were reached. Three replicate measurements of negative and positive ion mass spectra were collected using full-scan analysis for the range of m/z values 100 to 1000 with the mass resolving power set at 400 000 (at m/z 400). In this paper, we report only the findings from the negative ion mode measurements. Automatic gain control was used to consistently fill the linear ion trap quadropole mass analyzer (LTQ) with the same number of ions ($n = 10^6$) for each acquisition and to avoid space charge effects from overfilling the mass analyzer. The instrument was externally calibrated in negative ion mode with a standard solution of sodium dodecyl sulfate and taurocholic acid. Mass accuracy for the spectra was < 2 ppm. For each sample, more than 200 individual mass spectra recorded in the time domain were collected and stored as transients using Thermo Xcalibur software.

2.3.3 Data processing and assignment of molecular formulas

The analysis of ambient aerosol by FT-ICR MS method yields thousands of elemental compositions per sample (e.g., Mazzoleni et al., 2010, 2012). The aim of data processing is to interpret and represent data in an understandable and clear form. Transient co-addition and molecular formula assignment of ultrahigh-resolution FT-ICR MS data was performed with Composer software (Sierra Analytics, Modesto, CA version 1.0.5) as described in detail in previous publications (Putman et al., 2010;

ACPD
14, 24753–24810, 2014

Mazzoleni et al., 2012). Briefly, 200 recorded transients were first co-added for improved analyte detection (Kujawinski et al., 2002; Stenson et al., 2003). Internal recalibration of the mass spectra was not done and the mass accuracy was sufficient to assign the majority of the detected ions. The molecular formula calculator was set to allow up to 100 carbon (C), 400 hydrogen (H), 100 oxygen (O), 3 nitrogen (N) and 1 sulfur (S) atoms per molecular formula composition. The molecular formula calculator is based on the PREDATOR algorithm (Blakney et al., 2011) and uses a Kendrick mass defect (KMD) analysis (Hughey et al., 2001) to sort ions into user-defined homologous series. Kendrick transformation (Kendrick, 1963) helps in identifying homologous series of compounds that differ in number of base units (e.g., CH_2, O_x where x is an integer > 0, and CH_2O) only. KMD for an elemental composition of a compound C observed in a mass spectrum containing base unit B (e.g., CH_2) can be calculated from Kendrick Mass (KM) as:

$$\mathrm{KM} = \mathrm{C(observed\ mass)} \cdot \frac{\mathrm{B(nominal\ mass)}}{\mathrm{B(exact\ mass)}} \quad (1)$$

$$\mathrm{KMD} = \mathrm{Nominal\ Kendrick\ Mass} - \mathrm{KM} \quad (2)$$

All molecular formulas presented here were assigned using the CH_2 homologous series. Note that accurate formula assignments can be achieved with molecular formula extensions other than CH_2 (e.g., Kujawinski and Behn, 2006). Homologous compounds that differ by number of base units only will have the same KMD. KMD for the entire mass spectrum and selected base unit can be visualized in a Kendrick mass plot, in which KMD is plotted vs. nominal Kendrick mass (NKM). This visual representation aids in recognition of elemental compositions of the same type and class.

A user-defined de novo cutoff for the homologous series is used in the molecular formula assignments. De novo cutoff is the m/z value above which the molecular formula assignments are made only for the ions that belong to homologous series starting below the cutoff. We used a two-step approach here following the work of Koch et al. (2007), who reported that unequivocal molecular formula assignments

ACPD
14, 24753–24810, 2014

can be determined for species having CHO elemental composition for masses up to 1000 Da with small measurement error (< 1 ppm). However, this is not possible for species with elemental compositions including N, S and other heteroatoms. Therefore, we performed the following two methods of molecular formula assignments. Method A: elemental composition including C, H, O, N and S with a de novo cutoff at m/z 500; and Method B: elemental composition including only C, H and O with de novo cut off at m/z 1000. The results presented here are the combination of both methods without double counting. An assignment threshold of six times the root mean square values of the signal-to-noise ratio between m/z 988–990 was applied to the data. These assignment thresholds were 0.9, 0.2 and 0.1 % for 9/24, 9/25 and and laboratory filter blank, respectively. For the three replicates of each sample measured by FT-ICR MS, only the molecular formula assignments found in all three replicate analyses were retained. Molecular formulas with measurement errors larger than 3 ppm were discarded. Chemical rules and assumptions for additional quality assurance of the assigned formulas were adopted from Koch et al. (2005) and are described in detail in Putman et al. (2012).

Structural properties of molecular formulas can be inferred from the hydrogen deficiency, which is defined as the difference between the number of H atoms in a molecule and its completely saturated acyclic analogue. This difference corresponds to the number of double bonds and rings in a molecule (McLafferty and Turecek, 1993; Lobodin et al., 2012) and is referred to as the double bond equivalents (DBE) for a molecule in the general form of $C_cH_hN_nO_oS_s$ as:

$$\mathrm{DBE}(C_cH_hN_nO_oS_s) = c - \frac{h}{2} + \frac{n}{2} + 1 \quad (3)$$

Another metric to estimate the degree of molecular saturation and structure is the aromaticity index (AI). AI is defined as the minimum number of C-C double bonds and rings required to rationalize these molecular features based on elemental composition (Koch and Dittmar, 2006). AI is calculated for $C_cH_hN_nO_oS_s$ molecular compositions by

ACPD
14, 24753–24810, 2014

taking into account the C bonds with heteroatoms as:

$$AI = DBE_{AI}/C_{AI} = (1 + c + o + s - 0.5 \cdot h)/(c - o - s - n) \quad (4)$$

The elemental composition from each of the molecular assignments, accessible with ultrahigh-resolution of FT-ICR MS, enables the calculation of their O/C, H/C and OM/OC ratios. O/C (H/C) elemental ratio is calculated as the ratio of the number of O (H) vs. C atoms directly from detected elemental composition. OM/OC ratio is calculated as the ratio between measured or estimated mass and calculated mass of carbon in assigned molecular formulas. Properties of samples can also be evaluated by relative abundance weighting, which is determined by Eqs. (5)–(8) for each elemental composition $C_cH_hN_nO_oS_s$:

$$O/C_w = \frac{\sum w_i \cdot O_i}{\sum w_i \cdot C_i} \quad (5)$$

$$H/C_w = \frac{\sum w_i \cdot O_i}{\sum w_i \cdot H_i} \quad (6)$$

$$DBE_w = \frac{\sum w_i \cdot DBE_i}{\sum w_i} \quad (7)$$

$$OM/OC_w = \frac{\sum w_i \cdot OM/OC_i}{\sum w_i} \quad (8)$$

where w_i is the relative abundance for each individual molecular formula i. The sum includes all molecular formula assignments in a sample or its subset. Error of the weighted values is calculated by propagating the standard deviation (1σ) of the relative abundance used to weight the values for the group (Mazzoleni et al., 2012; Zhao et al., 2013).

ACPD
14, 24753–24810, 2014

2.4 FLEXPART particle dispersion model

Air mass history was determined using the Lagrangian particle dispersion model (LPDM) FLEXPART (version 8.2, Stohl et al., 1998). FLEXPART was used to determine the air mass history of plumes arriving at the PMO by simulating the release of thousands of passive tracer air parcels at the PMO location and advecting them backwards in time, providing a representation of the spatial distribution of the air mass at an upwind time referred to as a "retroplume". The meteorology dataset was comprised of a combination of 6 h meteorological final analysis data at 00:00, 06:00, 12:00, and 18:00 UTC, and 6 h Global Forecast System data at 03:00, 09:00, 15:00, and 21:00 UTC. All other model settings matched those used in Owen et al. (2006).

Retroplumes were also combined with anthropogenic and fire CO emission inventories to predict plume sources and ages (Owen and Honrath, 2009). For each upwind period, the portion of each retroplume in the 0–300 m layer was multiplied with the emission inventory to compute contributions of both emission types.

3 Results and discussion

3.1 Chemical characterization of the Pico Mountain Observatory samples

The analysis of the bulk chemical composition of filter-collected samples during 2012 shows that organic compounds often comprised the largest mass fraction of total aerosol, as presented by an overview in Table 1. Measured OC was converted to OM using the OM/OC ratio of 1.8 adopted from Pitchford et al. (2007) representing the literature consensus for remote areas. After blank subtraction, the average ambient mass concentration (± standard deviation, 1σ) of filter-collected species ($OM + EC + SO_4^{2-} + NO_3^- + Cl^-$) at the PMO during 2012 was $0.9 \pm 0.6\,\mu g\,m^{-3}$. On average, organics represent the largest mass fraction of the total measured aerosol species (57 ± 21 %) followed by sulfate (21 ± 12 %), nitrate (17 ± 14 %), chloride (3 ± 4 %), and EC

ACPD
14, 24753–24810, 2014

(2 ± 2 %). Figure 1a gives an overview of chemical composition of aerosol collected on filters at PMO during summer 2012. The OM/OC ratio of 1.8 adopted in our analysis is slightly higher than the OM/OC ratio of ∼ 1.7 calculated from FT-ICR MS analysis of WSOC elemental compositions (Table 2). As described in Mazzoleni et al. (2010), the elemental composition of each of the assigned molecular formulas enables calculation of OM/OC ratios. However, since the highly oxygenated low molecular weight species (MW ≤ 100) are not well retained on the SPE column, they would not be detected and thus were not part of the calculated OM/OC ratios. This can lead to somewhat lower OM/OC ratios than those determined using other methods (e.g., Hallar et al., 2013 and references therein). Therefore, an OM/OC value of 1.8 is appropriate for use here and might be the lower limit of OM/OC.

Figure 1b–d shows continuous measurements of BC mass concentration, the aerosol light scattering coefficient and number concentration for time periods overlapping with the filter-collection periods. We averaged those aerosol measurements over the filter-collection sampling periods (Fig. 1a), and the average BC mass concentration varies between 0.82 and 74 ng m^{-3} (Table 1), the average light scattering coefficient varies between 0.2 and 16.3 M m^{-1}, while the particle number varies between 0.3 and 21 particles m^{-3}. Correlations between total filter-collected aerosol mass and on-line aerosol measurements are very good, as shown in Supplement Fig. S2 (with an r^2 of 0.80, 0.90 and 0.93 for BC mass concentration, the aerosol light scattering coefficient and number concentration, respectively). This indicates that these three very different types of aerosol measurements captured the same trends during the overlapping sampling periods (Fig. 1).

3.2 Characterization of air masses during 24–26 September 2012

This section explains the choice of two filter-collected samples for detailed molecular characterization by ultrahigh-resolution FT-ICR MS. The two samples are named 9/24 and 9/25 representing the date when sampling of each filter started. The filter-collection period for 9/24 is 24 September 2012 at 15:00–25 September 2012 at 15:00

ACPD
14, 24753–24810, 2014

and for 9/25 is 25 September 2012 at 15:00–26 September 2012 at 15:00 (Table 2). In this paper, unless noted otherwise, "9/24" and "9/25" always refer to the filter samples collected during these time periods.

An increase in the measured aerosol mass concentration and light scattering was observed during September 2012. As shown in Fig. 1, the highest loading of filter-collected aerosol was observed in 9/24, followed by decreased mass concentrations in 9/25. Similar trends were also observed for the continuous measurements (Fig. 1b–d) of BC mass concentration, aerosol light scattering and particle count. The observed values were much higher than during other periods overlapping with the daily filter measurements. The observed elevated aerosol concentrations are explained by the arrival of air masses from North America with biomass burning influenced aerosol. September 2012 was a dry month and several US states were experiencing a period of intense drought (NOAA National Climatic Data Center, 2012). Consequently, widespread wildfires were observed in the US northwest and northern Rockies (e.g., Idaho, Montana, Washington and Oregon). While the monthly number of wildfires of 3734 was the 2nd lowest during 2000–2012 observation period, the average monthly fire size was the 2nd highest for the same period with a total burn area of 1 077 766 acres. The wildfire activity during September 2012 in the northwestern US is corroborated by the Moderate Resolution Imaging Spectroradiometer (MODIS) satellite daily fire counts in Supplement Fig. S3 (NASA and University of Maryland, 2002), which also shows that the most intense wildfire activity was in the northwestern US (Fig. S3 in the Supplement). The Level 3 Aerosol Optical Depth (AOD) Dark-Target (Levy et al., 2007) products ($1^{\circ} \times 1^{\circ}$) retrieved by MODIS Terra/Aqua at 550 nm (http://disc.sci.gsfc.nasa.gov/giovanni) indicate a large increase in AOD from mid to late September over northwestern US (data not shown), suggesting an increase in aerosol load over the northwestern US during this period, coinciding with the fire counts.

The FLEXPART retroplumes also support our findings, indicating different aerosol compositions and mass concentrations in the two samples. The resulting retroplumes show that the transport patterns changed tremendously within 48 h and thus brought

ACPD
14, 24753–24810, 2014

air masses with different chemical signatures to the PMO (retroplumes representative for the two measurement periods, and all retroplumes during 9/24 and 9/25 are given in Figs. 2 and Supplement Figs. S4 and S5, retrospectively). During the measurement period of the 9/24 sample (retroplumes are shown in Fig. S4 in the Supplement), the average modeled age of the CO associated with this plume was 12 days. A large portion of the retroplumes intersects the northwestern US regions of intense wildfires activity during 13–15 September 2012 (Fig. 2 and Supplement Fig. S3). A few retroplumes (Supplement Fig. S4e–g) were lifted to the free troposphere within the next day and encountered a high pressure system before arriving at PMO. Retroplumes during the 9/25 sample collection (Fig. S5 in the Supplement) have a CO tracer age of 15 days and are characterized by gradual shift of the transport heights from the middle free troposphere to the marine boundary layer and lack of influence from the US. For example, retroplumes subsided drastically and entered marine boundary two days before arriving at PMO (Supplement Fig. S5e–h). Therefore, the air masses arriving at PMO during the measurement period of 9/24 are highly influenced by the US biomass burning, while the ones that arrived during 9/25 are more strongly influenced by the marine boundary layer. Simulated contributions of FLEXPART CO from various sources during September 2012 are given in Supplement Fig. S6.

We also examined the occurrence of upslope flow due to mechanical lifting during September 2012 by using the same methodology as Zhang et al. (2014). No occurrence of upslope flow was observed for the period of 24–26 September 2012 selected for detailed study in this work. This suggests that filter-collected samples during those dates were not affected by local emissions due to mechanically lifted upslope flow.

3.2.1 Non-methane hydrocarbon measurements

Measurements of gas-phase species such as NMHC and ozone for 24–26 September offer additional means to determine the origin of air masses sampled at the observatory. Methods for the NMHC and ozone measurements have been described in detail elsewhere (Helmig et al., 2008; Tanner et al., 2006; Oltmans and Levy II, 1994). The

ACPD
14, 24753–24810, 2014

observed change in the air masses during filter measurements of 9/24 and 9/25 is supported by the measurements of ethane and propane in Fig. 3e, which are shown together with the filter-measured species and continuous aerosol measurements for comparison (Fig. 3a–d). Ethane and propane mixing ratios increased during the measurement period of the 9/24 sample and decreased during the measurement period of the 9/25 sample. As shown, the mixing ratio of ethane (propane) increased from 0.78 (0.09) ppbv at 19:20 in the evening of 24 September to a maximum of 1.25 (0.22) ppbv at 09:30 in the morning of 25 September. This was followed by a clear decrease in ethane and propane to average mixing ratios of 0.76 and 0.06, respectively, during the measurement period of the 9/25 sample. Decreases in NMHC mixing ratios were also evident in a drop of ln(propane/ethane) (Fig. 3e). The same trend was observed in the ozone mixing ratios during the case study period (Fig. 3f). The decreases in ethane, propane, and ozone mixing ratios, as well as in ln(propane/ethane) suggest a significant change in the air masses transport and history, from less aged and more polluted air masses during measurement period of 9/24 to more aged and cleaner during measurement period of 9/25. The full record of gas-phase species mentioned above and measured during periods overlapping with Hi-Vols sampling is shown in Supplement Fig. S7.

3.2.2 Scanning electron microscopy (SEM) analysis

Representative SEM images for 9/24 and 9/25 are shown in Fig. 4a and b, respectively. Over 2000 individual particles from each of the 9/24 and 9/25 samples were classified based on their morphology to investigate relative abundance of spherical particles. A higher fraction of spherical particles was observed on 9/24 (~ 43 %) compared to 9/25 (~ 18 %). However, the fraction of near spherical particles was slightly lower on 9/24 (~ 23 %) compared to 9/25 (~ 29 %). The spherical particles observed on 9/24 and 9/25 are likely tar balls (TBs) (Fig. 4c–d). TB are spherical, organic amorphous particles composed of carbon and oxygen and one of the major types of particles in biomass burning aerosol (Adachi and Buseck, 2011; China et al., 2013;

ACPD
14, 24753–24810, 2014

Pósfai et al., 2003, 2004; Tivanski et al., 2007). The EDS analysis of spherical and near spherical particles shows that they are mostly composed of C and O, consistent with the hypothesized identification. The diameter range of the TBs observed for fresh (minutes to ∼ 1 h aged) biomass burning plumes is typically 30 to 500 nm (Adachi and Buseck, 2011; Pósfai et al., 2004), while a broader range (50–1600 nm) is observed for relatively aged (∼ 1–2 h aged) plumes (China et al., 2013). The TBs observed here have diameters in the range of 70–1800 nm and a plume age > 12 days. The relative abundance of TBs depends on the plume age. For example, fractions of TBs up to 90 % have been reported in 1–2 h aged plumes (China et al., 2013; Hand et al., 2005; Pósfai et al., 2003, 2004), but smaller fractions of TBs (∼ 15 %) have been observed in fresh aerosol (Adachi and Buseck, 2011). As described by China et al. (2013), up to 50 % of soot particles emitted from biomass burning are heavily coated (embedded) with other material. Thus, we visually classified the soot particles for 9/24 and 9/25 (N = 433 and 550, respectively) using the classification described by China et al. (2013) to investigate if the mixing of the soot after long-range transport was heavily coated (embedded soot), partly coated, thinly coated, or mixed/attached with other material (soot-inclusion). We found that ∼ 46 % of the soot particles with respect to the total number of classified soot particles of 9/24 were heavily coated (Fig. 4e–h) compared to ∼ 17 % only in 9/25. The higher fraction of heavily coated soot particles observed for 9/24 suggests that the air mass on 9/24 was most likely influenced by a biomass burning plume. The fractions of other types of mixing for classified soot particles for 9/24 and 9/25 are 34 and 58 % for partly coated, 11 and 17 % for bare and 7 and 8 % for soot-inclusion.

The SEM analysis presented in this work was performed to investigate the typical morphology of particles collected during 24–26 September 2012 case study and their possible sources. Note that the spherical particles (possibly tar balls) detected by SEM analysis during the case study are not likely to be water-soluble. Therefore, the ultra-high resolution mass spectrometry analysis of WSOC compounds presented below probably does not probe them.

ACPD
14, 24753–24810, 2014

3.3 Molecular level characterization of the 9/24 and 9/25 samples

3.3.1 Mass spectra and molecular formula assignments

The exact mass measurements of the ultrahigh resolution FT-ICR MS allow for unequivocal molecular formula assignments of WSOC in the form of $C_cH_hN_nO_oS_s$, where c, h, n, o and s are numbers of C, H, N, O and S atoms. Molecular formulas were assigned to 68–78 % of the total ion current depending on the sample and whether the assignment of molecular formulas was performed by method A or B. The three replicate measurements of 9/24 and 9/25 analyzed by method A with C, H, N, O and S resulted in 72 and 78 % assignments of total ion current. Additional molecular formulas at the higher m/z values were assigned with method B for species containing C, H and O only. When methods A and B were combined, the assignments yielded a total of 3960 and 4770 monoisotopic molecular formulas for 9/24 and 9/25 (Table 2). Polyisotopic formula assignments containing naturally occurring ^{13}C and ^{34}S were also detected in aerosol samples. The vast majority of all assigned monoisotopic formulas contains corresponding ^{13}C assignments (91–95 %), while 69–100 % of ^{32}S-containing monoisotopic ions also contain formula assignments with ^{34}S, consistent with previous findings (e.g., Mazzoleni et al., 2012).

The reconstructed mass spectra of molecular formulas assigned to 9/24 and 9/25 WSOC (Fig. 5) indicate a high isobaric complexity due to the large number of monoisotopic anions (Table 2). Examples of the isobaric complexity are illustrated for the range of m/z 409.0–409.3 (Fig. 5c and g) with 12 and 21 molecular assignments for 9/24 and 9/25. Mass spectra of both WSOC samples are characterized by high m/z values with maximum relative abundance of detected ions in the range of m/z 400–500. Approximately 2/3 of all detected molecular assignments are found at high $m/z > 400$. This is a unique feature of the WSOC at PMO that has not been observed in other samples analyzed with FT-ICR MS. Previously, maximum relative abundance of molecular assignments detected in aerosol (Wozniak et al., 2008; Schmitt-Kopplin et al., 2010; Mazzoleni et al., 2012) and cloud water (Zhao et al., 2013) were observed between

ACPD
14, 24753–24810, 2014

m/z 200–400. Moreover, WSOC samples collected from various other locations do not have a significant number of compounds detected above m/z 400 (e.g., Wozniak et al., 2008; Mazzoleni et al., 2010). The higher molecular weight ranges observed in PMO WSOC samples are likely a result of the aging processes during the long-range transport.

The assigned molecular formulas were divided into four groups based on their elemental composition and named after the atoms included: CHO, CHNO, CHOS and CHNOS. The highest number of molecular assignments were CHO group species, which account for ∼ 70 % of the total number of assigned species (Table 2). CHO species have the highest observed relative abundance values with a maximum in the range of m/z 400–500 (Fig. 5). All molecular formulas assigned to the CHO group in both samples were characterized by distinct spacing of CH_2 homologous series. The second most abundant group of species was CHNO with ∼ 26 % of molecular assignments (Table 2). The maximum relative abundance of the CHNO group was at slightly higher m/z values compared to CHO compounds. We observed a surprisingly small number of S containing species. There were 14 and 289 CHOS molecular formulas in 9/24 and 9/25, representing 0.4 and 6 % of all assignments. The CHOS species detected in 9/24 had low relative abundance and only two ions had relative abundance > 1.5 % ($C_{12}H_{26}SO_4$ and $C_{14}H_{30}SO_4$). Most of the CHOS assignments in 9/25 also had low relative abundance (< 2 %), but 12 have relative abundance > 5 %. Finally, a very small number of low relative abundance CHNOS compounds were detected in 9/24 and 9/25 ($N = 7$ and 28). It is not likely that nitrooxy organosulfates will be observed after long-range transport, especially given that WSOC compounds contain such a small number of S containing species. Thus, the CHNOS molecular formula assignments were not included in the analysis presented here.

Overall, the Kendrick plots of the molecular assignments for the two samples (Fig. 6a and c) have higher values of both KMD and NKM with a narrower distribution compared to Zhao et al. (2013). This narrow and uniform distribution has not been observed in other Kendrick plots of aerosol WSOC (e.g., Kourtchev et al., 2013) and may be an

ACPD
14, 24753–24810, 2014

indication of highly processed aerosol. Ultrahigh-resolution FT-ICR MS measurements of a Suwannee River Fulvic Acid standard, a model for HULIS, yield very similar distribution in the Kendrick plot (Stenson et al., 2003), confirming the very aged and processed nature of PMO aerosol WSOC. Due to the presence of thousands of molecular assignments, it is difficult to see the details of the Kendrick plot. Therefore, Fig. 6b shows an excerpt of the Kendrick plot for 9/24 in order to illustrate the molecular complexity. Numerous molecular assignments are apparent and the separation in homologous series is evident with the same KMD differing by number of CH_2 base units only. As examples, we highlighted three homologous series belonging to the CHO, CHNO and CHOS groups: $(CH_2)_{1-19}C_3H_4O_4$, $(CH_2)_{1-5}C_6H_3NO_2$, and $(CH_2)_{1-2,5,7}C_7H_{16}SO_4$, respectively.

The molecular formulas of ions in the FT-ICR mass spectrum can be accurately calculated due to its high resolution and accuracy; this enables the calculation of elemental ratios. This is visualized using van Krevelen diagrams (Kim et al., 2003) with the H/C ratio plotted against the O/C, or N/H or S/H ratio (Wu et al., 2004). The van Krevelen diagrams for the 9/24 and 9/25 in Figs. 6d and f show a narrow and homogeneous distribution with aliphatic and olefinic species (Table 2). For example, the range of values of O/C ratio for aerosol WSOC collected at the PMO vs. the Storm Peak Laboratory (Mazzoleni et al., 2012) is 0.13–1.48 vs. 0.07–1.80. As discussed in the following sections, this tight distribution might be characteristic of very processed aerosol. Molecular assignments in the van Krevelen diagram are aligned to lines reflecting different chemical trends and reactions. Examples of those lines are visualized in Fig. 6e, including: (i) saturation or unsaturation, (ii) oxidation or reduction; and (iii) functionalization (i.e., alkylation in this diagram) or fragmentation. Mass resolved H/C diagrams are given in Fig. S8 in the Supplement to confirm the quality of molecular assignments of ultrahigh-resolution FT-ICR mass spectra. The similarity in the distributions of species in the mass resolved H/C diagram reported here to those reported previously (Schmitt-Kopplin et al., 2010) is noted and further discussed in the sections below.

ACPD
14, 24753–24810, 2014

DBE (Eq. 3) and AI (Eq. 4) values help in inferring the structures of the molecular formulas. The DBE for 9/24 and 9/25 cover a wide range of values (Figs. 6g and 6i) consistent with the molecular complexity of the samples described above. The distribution of molecular assignments in DBE vs. number of carbon atoms is both wide and uniform, which might be characteristic for highly aged and processed aerosol. Numerous homologous series of species overlap at each DBE value. Figure 6h highlights examples of homologous series with DBE values of 10–12 for CHO ($C_{14}H_{10}O_{10}$ $(CH_2)_n$, $C_{15}H_{10}O_{11}$ $(CH_2)_n$ and $C_{14}H_6O_7$ $(CH_2)_n$), and CHNO groups ($C_{14}H_{11}NO_{10}$ $(CH_2)_n$, $C_{16}H_{13}NO_{11}$ $(CH_2)_n$ and $C_{16}H_{11}NO_{11}$ $(CH_2)_n$). AI analysis of PMO WSOC supports the observations from the elemental ratios and DBE values. In both samples, most of the species have aliphatic (~55 %) and olefinic (~40 %) character with only a small contribution from aromatic species (~5 %) (Table 2). This finding is in agreement with previous studies of ambient aerosol (Schmitt-Kopplin et al., 2010; Mazzoleni et al., 2010, 2012; LeClair et al., 2012), which also found that a majority of species have aliphatic and olefinic character.

3.3.2 Molecular formulas assignments of the CHO group

The CHO species presented in the isoabundance van Krevelen diagram (Fig. 7a and b) for 9/24 and 9/25 have average O/C ratios of 0.47 and 0.42 and average H/C ratios of 1.19 and 1.28 (Table 2). Overall, the range of observed O/C ratios is 0.1–1.5 and the range for H/C ratios is 0.4–2.2. The highest relative abundance species in 9/24 are near O/C ~ 0.5 and H/C ~ 1.1 and those in 9/25 are near O/C ~ 0.4 and H/C ~ 1.2. There are eight low relative abundance (< 3 %) molecular assignments with an O/C ≥ 1 in each sample. Both samples have a wide distribution of elemental ratios around the maximum in the van Krevelen diagrams. The distribution of elemental ratios of the CHO group is similar to the aerosol samples reported by Mazzoleni et al. (2012) and much tighter than the cloud water samples reported by Zhao et al. (2013) measured at the Storm Peak Laboratory.

ACPD
14, 24753–24810, 2014

The DBE of the CHO molecular assignments for PMO samples (Fig. 7c and d) spans a wide range of values (0–19) and increases with the carbon number. The average DBE values are 10.8 and 9.8 for 9/24 and 9/25. The average DBE values of CHO compounds are much higher than the average DBE values of ∼ 6 observed in studies of WSOC in continental samples (Mazzoleni et al., 2012; Lin et al., 2012a; Zhao et al., 2013), which indicates they are more unsaturated. The CHO species are equally distributed among the range of DBE values with the highest relative abundance species in 9/24 and 9/25 found between DBE 5–14 and 3–14. The high relative abundance compounds (relative abundance ≥ 10 %) of 9/24 have 7–30 carbon atoms and the highest relative abundance compounds (relative abundance ≥ 20 %) have molecular assignments with 17–24 carbon atoms (Fig. 7c). DBE values of 9/25 follow a similar pattern (Fig. 7d) and its high relative abundance CHO compounds have 8–31 carbon atoms (relative abundance ≥ 5 %), with the highest relative abundance compounds (relative abundance ≥ 10 %) among molecular assignments having 12–26 carbon atoms. Clearly, the highest relative abundance CHO species of 9/25 have a wider distribution of DBE values than those on 9/24. The weighted O/C ratios of 0.47 and 0.43 for the CHO group (Table 2) of 9/24 and 9/25 are similar to those observed for other samples collected at the Storm Peak Laboratory, a high-altitude observatory near Steamboat Springs, CO, USA. Mazzoleni et al. (2012) reported a value of 0.48 for aerosol samples and Zhao et al. (2013) reported a value of 0.47 for cloud water samples both from the Storm Peak Laboratory. A slightly higher O/C ratio of ∼ 0.5 was observed for fog water samples collected in Fresno, CA (Mazzoleni et al., 2010). The weighted H/C ratios for 9/24 and 9/25 observed in this work are 1.17 and 1.26, which is lower than previous values of ∼ 1.5 reported for WSOC samples of aerosol (Wozniak et al., 2008; Mazzoleni et al., 2012), cloud water (Zhao et al., 2013), fog water (Mazzoleni et al., 2010), and rainwater (Altieri et al., 2009a). The low H/C and high DBE values suggest a higher degree of unsaturation for PMO samples and this is in agreement with longer aging times during which processing can lead to more SOA formation (Ng et al., 2011). The O/C ratios of PMO samples are consistent with those reported for aged biomass

ACPD
14, 24753–24810, 2014

burning aerosol measured by an Aerodyne Aerosol Mass Spectrometer (AMS) (Aiken et al., 2008). Ultrahigh resolution MS elemental ratios have been found to both agree (Bateman et al., 2012) and disagree (O'Brien et al., 2013) with the ones measured by an AMS, although a direct comparison of elemental ratios measured by FT-ICR MS and AMS has not yet been reported.

A number of molecular formulas matching biomass burning markers (Simoneit, 2002) were observed in PMO samples. Burning products of biopolymers such as cellulose, lignin and lignans can represent major amounts of OA originating from biomass burning. Levoglucosan is one of the main particle-phase markers of cellulose decomposition and its molecular formula ($C_6H_{10}O_5$) was observed with relative abundance values of 3.4 and 0.6 % in 9/24 and 9/25. Note this formula could come from other compounds having the same molecular formula such as galactosan and mannosan (Simoneit et al., 2001). In both 9/24 and 9/25 we also observed formulas that could be lignin pyrolysis products such as vanillic acid ($C_8H_8O_4$; relative abundance = 11.1 and 2.0 %), syringaldehyde ($C_9H_{10}O_4$; relative abundance = 9.2 and 2.0 %) and syringic acid ($C_9H_{10}O_5$; relative abundance = 7.3 and 1.4 %). In all cases, higher relative abundance values were observed in the mass spectra of 9/24. Burning of the lignin produces phenol (C_6H_6O), guaiacol (2-methoxyphenol; $C_7H_8O_2$) and syringol (1,3-dimethoxyphenol; $C_8H_{10}O_3$) (Simoneit, 2002). Phenols can also be formed in the atmosphere by oxidation of aromatics and HULIS (Graber and Rudich, 200). These molecular formulas were found in 9/24 and 9/25 with higher relative abundance on 9/24, including: phenol (relative abundance = 3.5 and 0.6 %), guaiacol (relative abundance = 2.8 and 0.7 %), and syringol (relative abundance = 7.0 and 1.5 %). Sun et al. (2010) observed that aqueous-phase oxidation of guaiacol and syringol yields a substantial fraction of dimers and higher oligomers. Key dimer markers were identified as $C_{16}H_{18}O_6$ and $C_{14}H_{14}O_4$. Their results indicated that fog and cloud processing of phenolic species could be an important mechanism for the production of low-volatility SOA. The dimer markers $C_{16}H_{18}O_6$ and $C_{14}H_{14}O_4$ are also present in PMO samples with high relative abundance (for 9/24: relative abundance = 14.1 and 8.1 %,

ACPD
14, 24753–24810, 2014

respectively; for 9/25: relative abundance = 4.4 and 2.4 %, respectively). This suggests that the samples collected at PMO were influenced by biomass burning aerosol, processed by clouds and remained in the particle-phase after the evaporation of water. Similar observations of aqueous-phase processing of biomass burning aerosol were previously reported for cloud water (Zhao et al., 2013) and fog water samples (Mazzoleni et al., 2010).

3.3.3 Molecular assignments of the CHNO group

Aerosol WSOC CHNO species collected at PMO have a tight distribution of elemental ratios in the isoabundance van Krevelen diagram (Fig. 8a and b). For 9/24, O/C and H/C ratios span the range of 0.2–0.75 and 0.6–1.6 with higher relative abundance molecular formulas (relative abundance ≥ 4 %) in the range of 0.3–0.6 and 0.8–1.4. Similar values were observed for 9/25. Average O/C ratios for 9/24 and 9/25 were 0.45 and 0.42 and average H/C ratios were 1.14 and 1.18. A comparison of the distribution of the CHO and CHNO molecular assignments in the van Krevelen diagrams (Figs. 7 and 8, respectively) shows that they are found in similar ranges. The CHNO species have an overall tighter distribution than CHO. Consequently, the average values of elemental ratios for CHO and CHNO species are similar for each sample, which may be an indication of the same emission sources and transformation processes. The O/C ratios of the CHNO compounds are lower than those previously observed for continental samples of fog (~ 0.5, Mazzoleni et al., 2010), aerosol (0.57, Mazzoleni et al., 2012) and cloud water (0.72, Zhao et al., 2013). Similarly, CHNO molecular species detected in continental rainwater samples (Altieri et al., 2009a, b) are more oxygenated (O/C = 1.6) and saturated (H/C = 1.9) than PMO aerosol WSOC. Lower elemental ratios of PMO WSOC might be a result of oxidation leading to increased molecular fragmentation due to the long-range transport of the collected aerosol. Rural aerosol collected at a ground site had elemental ratios similar to those reported here, and might have been influenced by biomass burning as indicated by the detection of marker species such as lignin and nitro-aromatics (Wozniak et al., 2008).

ACPD
14, 24753–24810, 2014

Likewise, Schmitt-Kopplin et al. (2010) reported similar elemental ratios for an aerosol sample collected during a biomass burning event. They observed a high abundance of CHNO species attributed to aromatic acids, lignins and SOA formation. The same work reports mass resolved H/C diagrams for biomass burning aerosol (Schmitt-Kopplin et al., 2010), which have a strong resemblance to those reported here for both PMO samples (Supplement Fig. S8a and b). A significant contribution of CHNO compounds was observed in aerosol collected in the Pearl River Delta region in China and was attributed to biomass burning HULIS and photochemically produced SOA (Lin et al., 2012a). The CHNO molecular assignments in their study have similar elemental ratios (O/C = 0.41 and H/C = 1.15) and an OM/OC ratio (1.80) as those described here and their composition was explained by the presence of nitro or nitrate groups. Similar to the findings of Lin et al. (2012a), we observed high O/N ratios (~ 8 on average) and nearly all CHNO compounds have O/N ≥ 3, indicating that nitrogen is in the form of organic nitrate ($-ONO_2$) or nitro ($-NO_2$) groups with excess oxygen forming additional oxygenated groups.

The DBE values for the CHNO molecular assignments cover a wide range from 4–17 for both samples (Fig. 8c and d). This range of DBE values represents CHNO species having carbon numbers up to 35. As expected, the DBE increased with the increase in the number of carbon atoms. CHNO molecular assignments with high relative abundance in 9/24 have 16–30 carbon atoms with DBE values in the range of 8–16. The most abundant CHNO species were those having 19–25 carbon atoms and DBE values in the range of 10–12. Similar characteristics were observed in 9/25. Finally, the average DBE values for CHNO molecular assignments in 9/24 and 9/25 are 10.3 and 9.8. Similar to the CHO compounds, the DBE values of PMO CHNO compounds are much higher than those observed for continental WSOC samples in other studies, confirming the unsaturation feature of the aerosol after long-range transport and the same emission source regions and transformational processes of CHO and CHNO group species.

ACPD
14, 24753–24810, 2014

In both PMO aerosol WSOC samples, we observed 1 or 2 nitrogen atoms (N_1 or N_2 molecular formulas, respectively) per CHNO molecular assignment although we allowed up to 3 nitrogen atoms per formula. In both samples, N_1 molecular formulas make up the majority of CHNO species (91 %), while N_2 molecular formulas represent only 9 %. In order to better understand this, we divided them according to their nitrogen and oxygen content. In this way, a distribution of the subclasses is observed and it is very similar for the two samples (Supplement Fig. S9). Figure S9 in the Supplement shows that for both samples N_1 and N_2 molecular assignments of CHNO species have up to 14 and 13, respectively, O atoms. For the N_1 species, the trend of the sum of relative abundance vs. oxygen number uniformly increases to its maximum of $\sim N_1O_{11}$ after which it drops off sharply. Nearly all molecular formulas in the N_1 and N_2 classes are enriched in oxygen (high O/N ratio), indicating the likely presence of organic nitrate or nitro groups.

3.3.4 Molecular formula assignments of the CHOS group

A small number of CHOS molecular assignments (N = 14 and 289 for 9/24 and 9/25) was observed and the majority of them had low relative abundance. CHOS molecular assignments in 9/24 have average O/C and H/C ratios of 0.5 and 1.75, respectively (Fig. 9a). The H/C ratio is significantly higher than those observed for CHO and CHNO compounds, indicating a higher degree of saturation. Relatively high saturation is confirmed by the significantly lower DBE values for the CHOS species (Fig. 9c). The range of DBE values is 0–7, with only three discrete DBE values (0, 4 and 7). Except for three molecular assignments ($C_{23}H_{34}O_9S$, $C_{19}H_{26}O_{10}S$, and $C_{19}H_{26}O_{11}S$), most of the CHOS compounds in 9/24 can be grouped into three CH_2 homologous series in the van Krevelen diagram (C_7H_{16} $(CH_2)_{1-2,5,7}O_4S$, $C_{14}H_{22}$ $(CH_2)_{1-4}O_{10}S$ and $C_{14}H_{22}$ $(CH_2)_{1-2,5}O_8S$). We note the presence of a very low number of CHOS assignments in 9/24.

The 9/25 sample has a substantially higher number of CHOS assignments (N = 289). The isoabundance van Krevelen diagram (Fig. 9b) shows that CHOS species

ACPD
14, 24753–24810, 2014

have a similar average O/C ratio and higher H/C ratio than CHO and CHNO ones. The range of O/C ratios for the CHOS species in this sample is 0.1–1.2 and the H/C ratio range is 0.9–2.2. The average elemental ratios are O/C = 0.41 and H/C = 1.7. The elemental ratios do not show a tight distribution in the van Krevelen diagram (Fig. 9b). Rather, we observe several groups of compounds following straight lines of CH_2 homologous series. The highest relative abundance corresponds to a fully saturated formula ($C_{12}H_{26}O_4S$), which is likely an organosulfate species. The higher relative abundance molecular formulas are found around the elemental ratios of O/C = 0.25 and H/C = 1.6, indicating a low degree of oxygenation and a high degree of saturation. Consistent with the higher saturation of these species, the DBE values are much lower than those observed for CHO and CHNO compounds (Fig. 9d). Molecular assignments with the highest relative abundance have a DBE of 0 and several species with high relative abundance are clustered around DBE values of 4 and 5. Figure S10 in the Supplement shows that the highest relative abundance species have four oxygen atoms and the relative abundance gradually decreases towards the maximum oxygen content of 13 oxygen atoms. The frequency distribution of the number of CHOS molecular assignments is similar to the oxygen content with a slight shift where the majority of species are found in O_5S and O_6S subclasses (N = 48 and 52, respectively).

Low DBE values and high O/S ratios indicate the presence of organosulfates similar to previous findings in samples of aerosol (Mazzoleni et al., 2012) and cloud water (Zhao et al., 2013). Consistent with Zhao et al. (2013), CHOS species do not form a tightly distributed group in the van Krevelen diagram (Fig. 9a and b) as observed for CHO (Fig. 7a and b) and CHNO (Fig. 8a and b). Similar to the previous study of Schmitt-Kopplin et al. (2010), we note the presence of several groups of CHOS species in the regions of the van Krevelen diagram attributed to fatty acids, oxidized terpenoids and aromatic acids from lignins. Those studies also found a group of highly unsaturated CHOS species with low O/C ratio that was attributed to aromatic moieties, which we did not observe here. The presence of organosulfates in fog water was confirmed by tandem mass spectrometry (MS/MS) analysis (LeClair et al., 2012).

ACPD
14, 24753–24810, 2014

Lin et al. (2012a) identified CHOS species in biomass burning aerosol with similar DBE values and higher O/C ratios compared to PMO CHOS species and attributed them to HULIS. Another study detected HULIS organosulfates (Lin et al., 2012b) and noted very few CHOS species in regional background aerosol samples collected at a mountaintop site. The lack of CHOS species was attributed to biomass burning and anthropogenic aerosol that were not sufficiently acidic to catalyze formation reactions of organosulfates. We find a similar low number of CHOS species in WSOC samples collected at PMO. Similarly, Schmitt-Kopplin et al. (2010) observed a lower number frequency of CHOS compounds than CHO and CHNO in biomass burning aerosol.

Oceanic marine algae produce dimethylsulfoniopropionate (DMSP), which is degraded by marine bacteria to dimethylsulfide (DMS). Once DMS is in the atmosphere, it is rapidly oxidized to aerosol sulfate via methanesulfonic acid and sulfur dioxide (Yoch, 2002). It is well documented that organosulfates can originate from the oxidation of marine biomass (O'Dowd et al., 1997; Rinaldi et al., 2010; Fu et al., 2011; Schmale et al., 2013). Nevertheless, the molecular-level speciation of marine aerosol organosulfates is sparse. Recently, Claeys et al. (2010) determined that the members of the $C_8H_{16}(CH_2)_{1-5}O_6S$ homologous series are the organosulfate markers of marine SOA formed from the oxidation and sulfation of algal and bacterial fatty acids residue. All of those molecular species except one ($C_9H_{18}O_6S$) are identified in 9/25. Moreover, the O_6S is the most abundant class in the CHOS group and the longest homologous series is $C_7H_{14}(CH_2)_{1,3-17}O_6S$ consistent with Claeys et al. (2010). Many other homologous series in the CHOS group were observed in 9/25 with long carbon chains (up to C_{32}) and high oxygen content (up to O_{13}) consistent with the oxidation and sulfation of primary marine biomass and subsequent additional processing during aging.

3.3.5 Comparison of the Pico Mountain Observatory aerosol samples

Overall, the molecular formulas assigned to 9/24 and 9/25 are quite similar. A total of 3426 molecular formulas are common for both samples and they span the entire m/z range (Fig. 10a–d). Molecular formulas unique for each sample are fewer ($N = 541$

ACPD
14, 24753–24810, 2014

and 1372 for 9/24 and 9/25) and most of the unique ions in both samples have low relative abundance. The highest relative abundance species in 9/24 were found in the range of m/z 450–700, while for 9/25 this range is from m/z 250–400. Similarly, the Kendrick plot analysis shows the unique assignments in 9/24 have homologous series preferentially extending to lower masses and those in 9/25 tend to form homologous series extending to higher masses (Fig. 10e).

The two WSOC samples are characterized by similar but not identical bulk properties. The average O/C ratio of 9/24 is slightly higher than 9/25 (0.46 vs. 0.42) indicating more oxygenation. In our previous study of a case similar to 9/24 that included substantial plume lofting to the middle free troposphere (Zhang et al., 2014), coupled GEOS-Chem and FLEXPART simulations suggested that similar transport patterns are capable of carrying more PAN in polluted plumes than non-lifted transport. The additional PAN is thus able to thermally decompose resulting in a significant NO_x release and subsequent ozone production during plume subsidence. This mechanism may have provided a second opportunity for efficient oxidation of the 9/24 aerosol. In contrast, NO_x and ozone production potential would quickly diminish in the marine boundary layer as shown by Zhang et al. (2014). In addition, air masses that transported the aerosol collected in 9/25 underwent longer transport times at substantially lower altitudes in cleaner marine atmosphere above the North Atlantic Ocean (9.5 days vs. 7 days in 9/24), which might have resulted in increased fragmentation of molecular species and a lower O/C ratio. Processing of different WSOC species from primary marine emissions would also explain the higher number of unique molecular assignments found in 9/25.

The average H/C ratio of 9/24 is slightly lower than that of 9/25 (1.17 vs. 1.28) indicating a lower average saturation. The van Krevelen diagram in Fig. 10f gives an overview of the differences in the two PMO samples and it shows that 9/24 molecular assignments have higher oxygenation (i.e., higher O/C) and unsaturation (i.e., lower H/C). A higher degree of unsaturation in 9/24 is also supported by higher DBE values (Table 2). The same trend in elemental ratios is also observed for CHO, CHNO and

ACPD
14, 24753–24810, 2014

CHOS group species. The exception to this is the higher H/C ratio of the CHOS group on 9/24, which might be due to the very low number of CHOS assignments. Approximately 70 % of the molecular assignments in both samples were CHO species and nearly all of the remaining compounds were CHNO species, so the overall elemental ratio characteristics will be strongly driven by these two groups. Note molecular formulas unique to 9/25 are located in the regions of the van Krevelen diagram (Fig. 10f) assigned to fatty acids (Schmitt-Kopplin et al., 2010) consistent with more abundant marine aerosol.

The average DBE values of 9/24 and 9/25 were 10.7 and 9.4 (Fig. 10g) and these values are similar to the average DBE found in the CHO and CHNO groups (Table 2). Much lower values were found for the CHOS group, consistent with a higher saturation of these species as noted previously. Figure 10g clearly shows the unique molecular assignments detected in 9/24 have higher DBE values, while those detected during 9/25 show more uniform distribution among all observed DBE values.

4 Conclusions

Chemical and physical characterization of free tropospheric aerosol at the Pico Mountain Observatory and molecular formulas assignment of aerosol WSOC were recently enabled with the installation of new instrumentation in 2012. The average ambient mass concentration of filter-collected aerosol of 0.9 $\mu g\,m^{-3}$ is in agreement with other measurements of free tropospheric aerosol mass. Our findings confirm the observations of OA dominance in the total aerosol mass fraction of remote atmospheres, followed by sulfate and nitrate aerosol. This work provides critical insights for aerosol in remote regions and at high-altitude observatories. Filter-collected aerosol data follow a trend similar to the continuous measurements of other aerosol properties and gas-phase species. Comparisons of filter-collected aerosol to on-line measurements of particle- and gas-phase species and meteorological parameters also add knowledge

ACPD
14, 24753–24810, 2014

on their emission sources and transformational processes and should continue in the future.

Ultrahigh resolution FT-ICR MS analysis of two WSOC samples collected during a pollution event yielded approximately 4000 and 5000 monoisotopic molecular formulas detected for 9/24 and 9/25. Compounds of CHO, CHNO and CHOS elemental groups were identified in both samples and ~ 70 and ~ 25 % of species were CHO and CHNO compounds, respectively. The CHOS group represented only a small number fraction. The average low O/C (~ 0.45) and H/C (~ 1.20) ratios indicate low oxygenation and low saturation, suggesting transformation processes leading to the fragmentation of aged SOA. The unsaturation may also be a result of the biomass burning emissions, which carry aerosol species more unsaturated than SOA products of some other compounds such as terpenes. Average DBE values (~ 10.5) and their range (0–19) indicate a high degree of functionalization characteristic of aged and processed aerosol. Many features observed for WSOC collected at PMO may suggest highly aged and processed aerosol. The FLEXPART simulations indicate that air masses intercepted during the measurements of 9/24 and 9/25 have plume ages of 12 and 15 days. However, the data for very aged ambient samples analyzed by ultrahigh resolution FT-ICR MS are sparse, which makes comparison of PMO WSOC samples difficult. Future research is needed to systematically characterize WSOC of different age, sources and transformational processes using ultrahigh resolution FT-ICR MS collected at PMO as well as at other locations.

The differences in the composition of the two samples were attributed to sampling of different air masses. FLEXPART retroplume analysis indicated that air masses intercepted at PMO during the 9/24 sample collection passed over North American areas with intense wildfire activity, while on 9/25 the air masses were more aged and spent more time residing over the North Atlantic Ocean. The differences in air masses are confirmed by changes in collocated on-line measurements of ozone, non-methane hydrocarbons (ethane and propane), and by BC mass concentration and aerosol number concentration and scattering coefficient. The air masses of 9/24 have higher transport

ACPD
14, 24753–24810, 2014

heights above the North Atlantic Ocean than those of 9/25, which might have allowed for increased production of oxidants such as ozone during their subsidence for 9/24. Increased oxidation of 9/24 WSOC also supports their observed higher oxygenation and unsaturation. Molecular level characterization of WSOC with FT-ICR MS enabled the identification of biomass burning molecular markers, their aqueous-phase oxidation products and marine aerosol. Biomass burning markers were present with higher relative abundance in 9/24, while organosulfates markers of marine aerosol were present only in 9/25. The tendency of several 9/25 compounds attributed to fatty acids and products of DMS oxidation supports the marine origin of these WSOC. The presence of a higher fraction of spherical particles (possibly tar balls) and a higher fraction of heavily coated soot suggests that 9/24 was more highly influenced by a biomass burning, consistent with the biomass burning markers observed in the molecular assignments.

The Supplement related to this article is available online at doi:10.5194/acpd-14-24753-2014-supplement.

Acknowledgements. This research was sponsored by the US National Science Foundation (AGS-1110059) and the US Department of Energy's Atmospheric System Research (DE-SC0006941). S. China was supported with a US National Aeronautics and Space Administration, Earth and Space Science Graduate Fellowship (#NNX12AN97H). Additional support was provided by Michigan Technological University (College of Sciences and Arts; Earth, Planetary and Space Sciences Institute and the Departments of Chemistry and Physics) for equipment cost share associated with the above grants. We thank the University of the Azores and the Regional Secretariat of the Environment and the Sea, Portugal for access to the station; the Pico mountain guides N. Nunes and J. Sergio of CUME 2351 Outdoor Experience for assistance with equipment transportation to the observatory; and M. Soule and E. Kujawinski of the Woods Hole Oceanographic Institution (WHOI) Mass Spectrometry Facility for FT-ICR MS data acquisition (NSF OCE-0619608 and Gordon and Betty Moore Foundation). We also thank E. Kane of the Michigan Technological University for assistance with the ion chromatography measurements; Senait Gebreeyesus of the Michigan Technological University for assistance

ACPD
14, 24753–24810, 2014

with the OC/EC measurements; and Audra McClure-Begley of NOAA Earth System Research Laboratory for analyzing and providing Pico ozone measurements.

References

Aiken, A. C., DeCarlo, P. F., Kroll, J. H., Worsnop, D. R., Huffman, J. A., Docherty, K. S., Ulbrich, I. M., Mohr, C., Kimmel, J. R., Sueper, D., Sun, Y., Zhang, Q., Trimborn, A., Northway, M., Ziemann, P. J., Canagaratna, M. R., Onasch, T. B., Alfarra, M. R., Prevot, A. S. H., Dommen, J., Duplissy, J., Metzger, A., Baltensperger, U., and Jimenez, J. L.: O/C and OM/OC ratios of primary, secondary, and ambient organic aerosols with high resolution time-of-flight aerosol mass spectrometry, Environ. Sci. Technol., 42, 4478–4485, 2008.

Adachi, K. and Buseck, P. R.: Atmospheric tar balls from biomass burning in Mexico, J. Geophys. Res., 116, D05204, doi:10.1029/2010JD015102, 2011.

Altieri, K. E., Turpin, B. J., and Seitzinger, S. P.: Oligomers, organosulfates, and nitrooxy organosulfates in rainwater identified by ultra-high resolution electrospray ionization FT-ICR mass spectrometry, Atmos. Chem. Phys., 9, 2533–2542, doi:10.5194/acp-9-2533-2009, 2009a.

Altieri, K. E., Turpin, B. J., and Seitzinger, S. P.: Composition of dissolved organic nitrogen in continental precipitation investigated by ultra-high resolution FT-ICR mass spectrometry, Environ. Sci. Technol., 43, 695–6955, 2009b.

Altieri, K. E., Hastings, M. G., Peters, A. J., and Sigman, D. M.: Molecular characterization of water soluble organic nitrogen in marine rainwater by ultra-high resolution electrospray ionization mass spectrometry, Atmos. Chem. Phys., 12, 3557–3571, doi:10.5194/acp-12-3557-2012, 2012.

Aumont, B., Szopa, S., and Madronich, S.: Modelling the evolution of organic carbon during its gas-phase tropospheric oxidation: development of an explicit model based on a self generating approach, Atmos. Chem. Phys., 5, 2497–2517, doi:10.5194/acp-5-2497-2005, 2005.

Bateman, A. P., Laskin, J., Laskin, A., and Nizkorodov, S. A.: Applications of high-resolution electrospray ionization mass spectrometry to measurements of average oxygen to carbon ratios in secondary organic aerosols, Environ. Sci. Technol., 46, 8315–8324, 2012.

Birch, M. E. and Cary, R. A.: Elemental carbon-based method for monitoring occupational exposures to particulate diesel exhaust, Aerosol Sci. Tech., 25, 221–241, 1996.

ACPD
14, 24753–24810, 2014

Blakney, G. T., Hendrickson, C. L., and Marshall, A. G.: Predator data station, a fast data acquisition system for advanced FT-ICR MS experiments, Int. J. Mass Spectrom., 306, 24–252, doi:10.1016/J.IJMS.2011.03.009, 2011.

Canagaratna, M., Jayne, J., Jimenez, J. L., Allan, J. A., Alfarra, R., Zhang, Q., Onasch, T., Drewnick, F., Coe, H., Middlebrook, A., Delia, A., Williams, L., Trimborn, A., Northway, M., DeCarlo, P., Kolb, C., Davidovits, P., and Worsnop, D.: Chemical and Microphysical Characterization of Ambient Aerosols with the Aerodyne Aerosol Mass Spectrometer, Mass Spectrom. Rev., 26, 185–222, 2007.

Carlton, A. G., Turpin, B. J., Altieri, K. E., Seitzinger, S. P., Mathur, R., Roselle, S. J., and Weber, R. J.: CMAQ model performance enhanced when in-cloud secondary organic aerosol is included: comparisons of organic carbon predictions with measurements, Environ. Sci. Technol., 42, 8798–8802, 2008.

China, S., Mazzoleni, C., Gorkowski, K., Aiken, A. C., and Dubey, M. K.: Morphology and mixing state of individual freshly emitted wildfire carbonaceous particles, Nat. Commun., 4, 2122, doi:10.1038/ncomms3122, 2013.

Claeys, M., Wang, W., Vermeylen, R., Kourtchev, I., Chi, X., Farhata, Y., Surratt, J. D., Gómez-González, Y., Sciare, J., and Maenhaut, W.: Chemical characterisation of marine aerosol at Amsterdam Island during the austral summer of 2006–2007, J. Aerosol Sci., 41, 13–22, 2010.

Dinar, E., Mentel, T. F., and Rudich, Y.: The density of humic acids and humic like substances (HULIS) from fresh and aged wood burning and pollution aerosol particles, Atmos. Chem. Phys., 6, 5213–5224, doi:10.5194/acp-6-5213-2006, 2006.

Dunlea, E. J., DeCarlo, P. F., Aiken, A. C., Kimmel, J. R., Peltier, R. E., Weber, R. J., Tomlinson, J., Collins, D. R., Shinozuka, Y., McNaughton, C. S., Howell, S. G., Clarke, A. D., Emmons, L. K., Apel, E. C., Pfister, G. G., van Donkelaar, A., Martin, R. V., Millet, D. B., Heald, C. L., and Jimenez, J. L.: Evolution of Asian aerosols during transpacific transport in INTEX-B, Atmos. Chem. Phys., 9, 7257–7287, doi:10.5194/acp-9-7257-2009, 2009.

Ervens, B. and Volkamer, R.: Glyoxal processing by aerosol multiphase chemistry: towards a kinetic modeling framework of secondary organic aerosol formation in aqueous particles, Atmos. Chem. Phys., 10, 8219–8244, doi:10.5194/acp-10-8219-2010, 2010.

Ervens, B., Turpin, B. J., and Weber, R. J.: Secondary organic aerosol formation in cloud droplets and aqueous particles (aqSOA): a review of laboratory, field and model studies, Atmos. Chem. Phys., 11, 11069–11102, doi:10.5194/acp-11-11069-2011, 2011.

ACPD
14, 24753–24810, 2014

Fialho, P., Hansen, A. D. A., and Honrath, R. E.: Absorption coefficients by aerosols in remote areas: a new approach to decouple dust and black carbon absorption coefficients using seven-wavelength Aethalometer data, J. Aerosol Sci., 36, 267–282, 2005.

Fialho, P., Freitas, M. C., Barata, F., Vieira, B., Hansen, A. D. A., and Honrath, R. E.: The Aethalometer calibration and determination of iron concentration in dust aerosols, J. Aerosol Sci., 37, 1497–1506, 2006.

Fu, P., Kawamura, K., and Miura, K.: Molecular characterization of marine organic aerosols collected during a round-the-world cruise, J. Geophys. Res., 116, D13302, doi:10.1029/2011JD015604, 2011.

Goldstein, A. H. and Galbally, I. E.: Known and unexplored organic constituents in the Earth's atmosphere, Environ. Sci. Technol., 41, 1514–1521, 2007.

Graber, E. R. and Rudich, Y.: Atmospheric HULIS: How humic-like are they? A comprehensive and critical review, Atmos. Chem. Phys., 6, 729–753, doi:10.5194/acp-6-729-2006, 2006.

Hallar, A. G., Lowenthal, D. H., Clegg, S. L., Samburova, V., Taylor, N., Mazzoleni, L. R., Zielinska, B. K., Kristensen, T. B., Chirokova, G., McCubbin, I. B., Dodson, C., and Collins, D.: Chemical and hygroscopic properties of aerosol organics at Storm Peak Laboratory, J. Geophys. Res., 118, 4767–4779, doi:10.1002/jgrd.50373, 2013.

Hallquist, M., Wenger, J. C., Baltensperger, U., Rudich, Y., Simpson, D., Claeys, M., Dommen, J., Donahue, N. M., George, C., Goldstein, A. H., Hamilton, J. F., Herrmann, H., Hoffmann, T., Iinuma, Y., Jang, M., Jenkin, M. E., Jimenez, J. L., Kiendler-Scharr, A., Maenhaut, W., McFiggans, G., Mentel, Th. F., Monod, A., Prévôt, A. S. H., Seinfeld, J. H., Surratt, J. D., Szmigielski, R., and Wildt, J.: The formation, properties and impact of secondary organic aerosol: current and emerging issues, Atmos. Chem. Phys., 9, 5155–5236, doi:10.5194/acp-9-5155-2009, 2009.

Hand, J. L., Malm, W. C., Laskin, A., Day, D., Lee, T., Wang, C., Carrico, C., Carrillo, J., Cowin, J. P., Collett, J., and Iedema, M. J.: Optical, physical, and chemical properties of tar balls observed during the Yosemite Aerosol Characterization Study, J. Geophys. Res., 110, D21210, doi:10.1029/2004JD005728, 2005.

He, F., Hendrickson, C. L., and Marshall, A. G.: Baseline mass resolution of peptide isobars: a record for molecular mass resolution, Anal. Chem., 73, 647–650, 2001.

Helmig, D., Tanner, D. M., Honrath, R. E., Owen, R. C., and Parrish, D. D.: Nonmethane hydrocarbons at Pico Mountain, Azores: 1. Oxidation chemistry in the North Atlantic region, J. Geophys. Res., 113, D20S91, doi:10.1029/2007JD008930, 2008.

ACPD
14, 24753–24810, 2014

Honrath, R. E., Owen, R. C., Val Martin, M., Reid, J. S., Lapina, K., Fialho, P., Dziobak, M. P., Kleissl, J., and Westphal, D. L.: Regional and hemispheric impacts of anthropogenic and biomass burning emissions on summertime CO and O_3 in the North Atlantic lower free troposphere, J. Geophys. Res., 109, D24310, doi:10.1029/2004JD005147, 2004.

Honrath, R. E., Helmig, D., Owen, R. C., Parrish, D. D., and Tanner, D. M.: Nonmethane hydrocarbons at Pico Mountain, Azores: 2. Event-specific analyses of the impacts of mixing and photochemistry on hydrocarbon ratios, J. Geophys. Res., 113, D20S92, doi:10.1029/2008JD009832, 2008.

Hughey, C. A., Hendrickson, C. L., Rodgers, R. P., Marshall, A. G., and Qian, K.: Kendrick Mass defect spectrum: a compact visual analysis for ultrahigh-resolution broadband mass spectra, Anal. Chem., 73, 4676–4681, 2001.

IPCC: Intergovernmental Panel on Climate Change, Climate Change 2013: The Scientific Basis, Cambridge University Press, Cambridge, England, 2013.

Jimenez, J. L., Canagaratna, M. R., Donahue, N. M., Prevot, A. S. H., Zhang, Q., Kroll, J. H., DeCarlo, P. F., Allan, J. D., Coe, H., Ng, N. L., Aiken, A. C., Docherty, K. D., Ulbrich, I. M., Grieshop, A. P., Robinson, A. L., Duplissy, J., Smith, J. D., Wilson, K. R., Lanz, V. A., Hueglin, C., Sun, Y. L., Tian, J., Laaksonen, A., Raatikainen, T., Rautiainen, J., Vaattovaara, P., Ehn, M., Kulmala, M., Tomlinson, J. M., Collins, D. R., Cubison, M. J., Dunlea, E. J., Huffman, J. A., Onasch, T. B., Alfarra, M. R., Williams, P. I., Bower, K., Kondo, Y., Schneider, J., Drewnick, F., Borrmann, S., Weimer, S., Demerjian, K., Salcedo, D., Cottrell, L., Griffin, R., Takami, A., Miyoshi, T., Hatakeyama, S., Shimono, A., Sun, J. Y., Zhang, Y. M., Dzepina, K., Kimmel, J. R., Sueper, D., Jayne, J. T., Herndon, S. C., Trimborn, A. M., Williams, L. R., Wood, E. C., Kolb, C. E., Middlebrook, A. M., Baltensperger, U., and Worsnop, D. R.: Evolution of organic aerosols in the atmosphere, Science, 326, 1525–1529, 2009.

Kanakidou, M., Seinfeld, J. H., Pandis, S. N., Barnes, I., Dentener, F. J., Facchini, M. C., Van Dingenen, R., Ervens, B., Nenes, A., Nielsen, C. J., Swietlicki, E., Putaud, J. P., Balkanski, Y., Fuzzi, S., Horth, J., Moortgat, G. K., Winterhalter, R., Myhre, C. E. L., Tsigaridis, K., Vignati, E., Stephanou, E. G., and Wilson, J.: Organic aerosol and global climate modelling: a review, Atmos. Chem. Phys., 5, 1053–1123, doi:10.5194/acp-5-1053-2005, 2005.

Kendrick, E.: A mass scale based on CH_2 = 14.0000 for high resolution mass spectrometry of organic compounds, Anal. Chem., 35, 2146–2154, 1963.

ACPD
14, 24753–24810, 2014

Kim, S., Kramer, R. W., and Hatcher, P. G.: Graphical method for analysis of ultrahigh-resolution broadband mass spectra of natural organic matter, the Van Krevelen Diagram, Anal. Chem., 75, 5336–5344, 2003.

Kleissl, J., Honrath, R. E., Dziobak, M. P., Tanner, D., Val Martin, M., Owen, R. C., and Helmig, D.: Occurrence of upslope flows at the Pico mountain top observatory: a case study of orographic flows on a small, volcanic island, J. Geophys. Res., 112, D10S35, doi:10.1029/2006JD007565, 2007.

Koch, B. P. and Dittmar, T.: From mass to structure: an aromaticity index for high-resolution mass data of natural organic matter, Rapid Commun. Mass Sp., 20, 926–932, doi:10.1002/RCM.2386, 2006.

Koch, B. P., Witt, M. R., Engbrodt, R., Dittmar, T., and Kattner, G.: Molecular formulas of marine and terrigenous dissolved organic matter detected by electrospray ionization fourier transform ion cyclotron resonance mass spectrometry, Geochim. Cosmochim. Ac., 69, 3299–3308, 2005.

Koch, B. P., Dittmar, T., Witt, M., and Kattner, G.: Fundamentals of molecular formula assignment to ultrahigh resolution mass data of natural organic matter, Anal. Chem., 79, 1758–1763, 2007.

Kourtchev, I., Fuller, S., Aalto, J., Ruuskanen, T. M., McLeod, M. W., Maenhaut, W., Jones, R., Kulmala, M., and Kalberer, M.: Molecular composition of boreal forest aerosol from Hyytiälä, Finland, using ultrahigh resolution mass spectrometry, Environ. Sci. Technol., 47, 4069–4079, 2013.

Kroll, J. H., Donahue, N. M., Jimenez, J. L., Kessler, S. H., Canagaratna, M. R., Wilson, K. R., Altieri, K. E., Mazzoleni, L. R., Wozniak, A. S., Bluhm, H., Mysak, E. R., Smith, J. D., Kolb, C. E., and Worsnop, D. R.: Carbon oxidation state as a metric for describing the chemistry of atmospheric organic aerosol, Nature Chem., 3, 133–139, doi:10.1038/nchem.948, 2011.

Kujawinski, E. B. and Behn, M. D.: Automated analysis of electrospray ionization fourier transform ion cyclotron resonance mass spectra of natural organic matter, Anal. Chem., 78, 4363–4373, 2006.

Kujawinski, E. B., Hatcher, P. G., and Freitas, M. A.: High-resolution fourier transform ion cyclotron resonance mass spectrometry of humic and fulvic acids, improvements and comparisons, Anal. Chem., 74, 41–419, 2002.

ACPD
14, 24753–24810, 2014

Kundu, S., Fisseha, R., Putman, A. L., Rahn, T. A., and Mazzoleni, L. R.: High molecular weight SOA formation during limonene ozonolysis: insights from ultrahigh-resolution FT-ICR mass spectrometry characterization, Atmos. Chem. Phys., 12, 5523–5536, doi:10.5194/acp-12-5523-2012, 2012.

Lapina, K., Honrath, R. E., Owen, R. C., Val Martin, M., and Pfister, G.: Evidence of significant large-scale impacts of boreal fires on ozone levels in the midlatitude Northern Hemisphere free troposphere, Geophys. Res. Lett., 33, L10815, doi:10.1029/2006GL025878, 2006.

Laskin, A., Laskin, J., and Nizkorodov, S. A.: Mass spectrometric approaches for chemical characterisation of atmospheric aerosols: critical review of the most recent advances, Environ. Chem., 9, 16–18, 2012.

LeClair, J. P., Collett, J. L., and Mazzoleni, L. R.: Fragmentation analysis of water-soluble atmospheric organic matter using ultrahigh-resolution FT-ICR mass spectrometry, Environ. Sci. Technol., 46, 4312–4322, 2012.

Levy, R. C., Remer, L. A., Mattoo, S., Vermote, E., and Kaufman, Y. J.: Second-generation algorithm for retrieving aerosol properties over land from MODIS spectral reflectance, J. Geophys. Res., 112, D13211, doi:10.1029/2006JD007811, 2007.

Lin, P., Rincon, A. G., Kalberer, M., and Yu, J. Z.: Elemental composition of HULIS in the Pearl River Delta region, China: results inferred from positive and negative electrospray high resolution mass spectrometric data, Environ. Sci. Technol., 46, 7454–7462, 2012a.

Lin, P., Yu, J. Z., Engling, G., and Kalberer, M.: Organosulfates in humic-like substance fraction isolated from aerosols at seven locations in East Asia: a study by ultra-high-resolution mass spectrometry, Environ. Sci. Technol., 46, 13118–13127, 2012b.

Lobodin, V. V., Rodgers, R. P., and Marshall, A. G.: Petroleomics and the analysis of complex organic mixtures with Fourier transform ion cyclotrone resonance, in: Comprehensive Environmental Mass Spectrometry, edited by: Lebedev, A. T., ILM Publications, a trading division of International Labmate Ltd., St. Albans, Hertfordshire, UK, 415–442, 2012.

Mazzoleni, L. R., Ehrmann, B. M., Shen, X., Marshall, A. G., and Collett Jr., J. L.: Water-soluble atmospheric organic matter in fog: exact masses and chemical formula identification by ultrahigh-resolution Fourier transform ion cyclotron resonance mass spectrometry, Environ. Sci. Technol., 44, 3690–3697, 2010.

Mazzoleni, L. R., Saranjampour, P., Dalbec, M. M., Samburova, V., Hallar, A. G., Zielinska, B., Lowenthal, D., and Kohl, S.: Identification of water-soluble organic carbon in nonurban

ACPD
14, 24753–24810, 2014

aerosols using ultrahigh-resolution FT-ICR mass spectrometry: organic anions, Environ. Chem., 9, 285–297, 2012.
McLafferty, F. W. and Turecek, F.: Interpretation of Mass Spectra, 4th Edn., University Science Books, Sausalito, CA, 1993.
Mead, R. N., Mullaugh, K. M., Brooks Avery, G., Kieber, R. J., Willey, J. D., and Podgorski, D. C.: Insights into dissolved organic matter complexity in rainwater from continental and coastal storms by ultrahigh resolution Fourier transform ion cyclotron resonance mass spectrometry, Atmos. Chem. Phys., 13, 4829–4838, doi:10.5194/acp-13-4829-2013, 2013.
NASA and University of Maryland: MODIS Hotspot/Active Fire Detections, Data set, MODIS Rapid Response Project, NASA/GSFC [producer], University of Maryland, Fire Information for Resource Management System [distributors], 2002.
Ng, N. L., Canagaratna, M. R., Jimenez, J. L., Chhabra, P. S., Seinfeld, J. H., and Worsnop, D. R.: Changes in organic aerosol composition with aging inferred from aerosol mass spectra, Atmos. Chem. Phys., 11, 6465–6474, doi:10.5194/acp-11-6465-2011, 2011.
Nguyen, T. B., Laskin, A., Laskin, J., and Nizkorodov, S. A.: Brown carbon formation from ketoaldehydes of biogenic monoterpenes, Faraday Discuss., 165, 473–494, doi:10.1039/C3FD00036B, 2013.
Nizkorodov, S. A., Laskin, J., and Laskin, A.: Molecular chemistry of organic aerosols through the application of high resolution mass spectrometry, Phys. Chem. Chem. Phys., 13, 3612–3629, 2011.
NOAA National Climatic Data Center, State of the Climate: Wildfires for September 2012, available at: http://www.ncdc.noaa.gov/sotc/fire/2012/9 (last access: 27 January 2014), 2012.
O'Brien, R. E., Laskin, A., Laskin, J., Liu, S., Weber, R., Russell, L. M., and Goldstein, A. H.: Molecular characterization of organic aerosol using nanospray desorption/electrospray ionization mass spectrometry: CalNex 2010 field study, Atmos. Environ., 68, 265–272, 2013.
O'Dowd, C. D., Smith, M. H., Consterdine, I. E., and Lowe, J. A.: Marine aerosol, sea-salt, and the marine sulphur cycle: a short review, Atmos. Environ., 31, 73–80, 1997.
Oltmans, S. J. and Levy II, H.: Surface ozone measurements from a global network, Atmos. Environ., 28, 9–24, 1994.
Owen, R. C. and Honrath, R. E.: Technical note: a new method for the Lagrangian tracking of pollution plumes from source to receptor using gridded model output, Atmos. Chem. Phys., 9, 2577–2595, doi:10.5194/acp-9-2577-2009, 2009.

ACPD
14, 24753–24810, 2014

Owen, R. C., Cooper, O. R., Stohl, A., and Honrath, R. E.: An analysis of the mechanisms of North American pollutant transport to the central North Atlantic lower free troposphere, J. Geophys. Res., 111, D23S58, doi:10.1029/2006JD007062, 2006.

Pfister, G. G., Emmons, L. K., Hess, P. G., Honrath, R. E., Lamarque, J. F., Val Martin, M., Owen, R. C., Avery, M. A., Browell, E. V., Holloway, J. S., Nedelec, P., Purvis, R., Ryerson, T. B., Sachse, G. W., and Schlager, H.: Ozone production from the 2004 North American boreal fires, J. Geophys. Res., 111, D24S07, doi:10.1029/2006JD007695, 2006.

Pitchford, M., Malm, W., Schichtel, B., Kumar, N., Lowenthal, D., and Hand, J.: revised algorithm for estimating light extinction from IMPROVE particle speciation data, J. Air Waste Manage., 57, 1326–1336, 2007.

Pósfai, M., Simonics, R., Li, J., Hobbs, P. V., and Buseck, P. R.: Individual aerosol particles from biomass burning in southern Africa: 1. Compositions and size distributions of carbonaceous particles, J. Geophys. Res., 108, 8483, doi:10.1029/2002JD002291, 2003.

Pósfai, M., Gelencsér, A., Simonics, R., Arató, K., Li, J., Hobbs, P. V., and Buseck, P. R.: Atmospheric tar balls: particles from biomass and biofuel burning, J. Geophys. Res., 109, D06213, doi:10.1029/2003JD004169, 2004.

Pratt, K. A. and Prather, K. A.: Mass spectrometry of atmospheric aerosols – recent developments and applications, Part I: Off-line mass spectrometry techniques, Mass Spectrom. Rev., 31, 1–16, 2012a.

Pratt, K. A. and Prather, K. A.: Mass spectrometry of atmospheric aerosols – recent developments and applications, Part II: On-line mass spectrometry techniques, Mass Spectrom. Rev., 31, 17–48, 2012b.

Putman, A. L., Offenberg, J. H., Fisseha, R., Kundu, S., Rahn, T. A., and Mazzoleni, L. R.: Ultrahigh-resolution FT-ICR mass spectrometry characterization of a-pinene ozonolysis SOA, Atmos. Environ., 46, 164–172, 2012.

Ramanathan, V., Li, F., Ramana, M. V., Praveen, P. S., Kim, D., Corrigan, C. E., Nguyen, H., Stone, E. A., Schauer, J. J., Carmichael, G. R., Adhikary, B., and Yoon, S. C.: Atmospheric brown clouds: hemispherical and regional variations in long-range transport, absorption, and radiative forcing, J. Geophys. Res., 112, D22S21, doi:10.1029/2006JD008124, 2007.

Reemtsma, T.: Determination of molecular formulas of natural organic matter molecules by (ultra-) high-resolution mass spectrometry: status and needs, J. Chromatogr. A, 1216, 3687–3701, 2009.

ACPD
14, 24753–24810, 2014

Remillard, J., Kollias, P., Luke, E., and Wood, R.: Marine boundary layer cloud observations in the Azores, J. Climate, 25, 7381–7398, 2012.
Rinaldi, M., Decesari, S., Finessi, E., Giulianelli, L., Carbone, C., Fuzzi, S., O'Dowd, C. D., Ceburnis, D., and Facchini, M. C.: Primary and secondary organic marine aerosol and oceanic biological activity: recent results and new perspectives for future studies, Adv. Meteorol., 2010, 310682, doi:10.1155/2010/310682, 2010.
Saxena, P. and Hildemann, L. M.: Water-soluble organics in atmospheric particles: a critical review of the literature and application of thermodynamics to identify candidate compounds, J. Atmos. Chem., 24, 57–109, 1996.
Schmale, J., Schneider, J., Nemitz, E., Tang, Y. S., Dragosits, U., Blackall, T. D., Trathan, P. N., Phillips, G. J., Sutton, M., and Braban, C. F.: Sub-Antarctic marine aerosol: dominant contributions from biogenic sources, Atmos. Chem. Phys., 13, 8669–8694, doi:10.5194/acp-13-8669-2013, 2013.
Schmitt-Kopplin, P., Gelencser, A., Dabek-Zlotorzynska, E., Kiss, G., Hertkorn, N., Harir, M., Hong, Y., and Gebefugi, I.: Analysis of the unresolved organic fraction in atmospheric aerosols with ultrahigh-resolution mass spectrometry and nuclear magnetic resonance spectroscopy: organosulfates as photochemical smog constituents, Anal. Chem., 82, 8017–8026, 2010.
Schmitt-Kopplin, P., Liger-Belair, G., Koch, B. P., Flerus, R., Kattner, G., Harir, M., Kanawati, B., Lucio, M., Tziotis, D., Hertkorn, N., and Gebefügi, I.: Dissolved organic matter in sea spray: a transfer study from marine surface water to aerosols, Biogeosciences, 9, 1571–1582, doi:10.5194/bg-9-1571-2012, 2012.
Shapiro, E. L., Szprengiel, J., Sareen, N., Jen, C. N., Giordano, M. R., and McNeill, V. F.: Light-absorbing secondary organic material formed by glyoxal in aqueous aerosol mimics, Atmos. Chem. Phys., 9, 2289–2300, doi:10.5194/acp-9-2289-2009, 2009.
Simoneit, B. R. T.: Biomass burning: a review of organic tracers for smoke from incomplete combustion, Appl. Geochem., 17, 129–162, 2002.
Simoneit, B. R. T. and Elias, V. O.: Detecting organic tracers from biomass burning in the atmosphere, Mar. Pollut. Bull., 42, 805–810, 2001.
Stenson, A. C., Marshall, A. G., and Cooper, W. T.: Exact masses and chemical formulas of individual suwannee river fulvic acids from ultrahigh resolution electrospray ionization Fourier transform ion cyclotron resonance mass spectra, Anal. Chem., 75, 1275–1284, 2003.

ACPD
14, 24753–24810, 2014

Stohl, A., Hittenberger, M., and Wotawa, G.: Validation of the Lagrangian particle dispersion model FLEXPART against large-scale tracer experiment data, Atmos. Environ., 32, 4245–4264, 1998.

Sun, Y. L., Zhang, Q., Anastasio, C., and Sun, J.: Insights into secondary organic aerosol formed via aqueous-phase reactions of phenolic compounds based on high resolution mass spectrometry, Atmos. Chem. Phys., 10, 4809–4822, doi:10.5194/acp-10-4809-2010, 2010.

Sun, Y., Zhang, Q., Zheng, M., Ding, X., Edgerton, E. S., and Wang, X.: Characterization and source apportionment of water-soluble organic matter in atmospheric fine particles ($PM_{2.5}$) with high-resolution aerosol mass spectrometry and GC-MS, Environ. Sci. Technol., 45, 4854–4861, 2011.

Tanner, D., Helmig, D., Hueber, J., and Goldan, P.: A gas chromatography system for the automated, unattended, and cryogen-free monitoring of C_2 to C_6 non-methane hydrocarbons in the remote troposphere, J. Chromatorgr. A, 1111, 76–88, 2006.

Tivanski, A. V., Hopkins, R. J., Tyliszczak, T., and Gilles, M. K.: Oxygenated interface on biomass burn tar balls determined by single particle scanning transmission X-ray microscopy, J. Phys. Chem. A, 111, 5448–5458, 2007.

Val Martin, M., Honrath, R. E., Owen, R. C., Pfister, G., Fialho, P., and Barata, F.: Significant enhancements of nitrogen oxides, black carbon, and ozone in the North Atlantic lower free troposphere resulting from North American boreal wildfires, J. Geophys. Res., 111, D23S60, doi:10.1029/2006JD007530, 2006.

Val Martin, M., Honrath, R. E., Owen, R. C., and Lapina, K.: Large-scale impacts of anthropogenic pollution and boreal wildfires on the nitrogen oxides over the central North Atlantic region, J. Geophys. Res, 113, D17308, doi:10.1029/2007JD009689, 2008a.

Val Martin, M., Honrath, R. E., Owen, R. C., and Li, Q. B.: Seasonal variation of nitrogen oxides in the central North Atlantic lower free troposphere, J. Geophys. Res., 113, D17307, doi:10.1029/2007JD009688, 2008b.

Wozniak, A. S., Bauer, J. E., Sleighter, R. L., Dickhut, R. M., and Hatcher, P. G.: Technical Note: Molecular characterization of aerosol-derived water soluble organic carbon using ultrahigh resolution electrospray ionization Fourier transform ion cyclotron resonance mass spectrometry, Atmos. Chem. Phys., 8, 5099–5111, doi:10.5194/acp-8-5099-2008, 2008.

Wu, Z., Rodgers, R. P., and Marshall, A. G.: Two- and three-dimensional van Krevelen diagrams: a graphical analysis complementary to the Kendrick Mass plot for sorting elemental composi-

ACPD
14, 24753–24810, 2014

tions of complex organic mixtures based on ultrahigh-resolution broadband Fourier transform ion cyclotron resonance mass measurements, Anal. Chem., 76, 2511–2516, 2004.

Yoch, D. C.: Dimethylsulfoniopropionate: its sources, role in the marine food web, and biological degradation to dimethylsulfide, Appl. Environ. Microb., 68, 5804–5815, 2002.

Zhang, B., Owen, R. C., Perlinger, J. A., Kumar, A., Wu, S., Val Martin, M., Kramer, L., Helmig, D., and Honrath, R. E.: A semi-Lagrangian view of ozone production tendency in North American outflow in the summers of 2009 and 2010, Atmos. Chem. Phys., 14, 2267–2287, doi:10.5194/acp-14-2267-2014, 2014.

Zhang, Q., Jimenez, J. L., Canagaratna, M. R., Allan, J. D., Coe, H., Ulbrich, I., Alfarra, M. R., Takami, A., Middlebrook, A. M., Sun, Y. L., Dzepina, K., Dunlea, E., Docherty, K., DeCarlo, P. F., Salcedo, D., Onasch, T., Jayne, J. T., Miyoshi, T., Shimono, A., Hatakeyama, S., Takegawa, N., Kondo, Y., Schneider, J., Drewnick, F., Borrmann, S., Weimer, S., Demerjian, K., Williams, P., Bower, K., Bahreini, R., Cottrell, L., Griffin, R. J., Rautiainen, J., Sun, J. Y., Zhang, Y. M., and Worsnop, D. R.: Ubiquity and dominance of oxygenated species in organic aerosols in anthropogenically-influenced Northern Hemisphere midlatitudes, Geophys. Res. Lett., 34, L13801, doi:10.1029/2007GL029979, 2007.

Zhao, Y., Hallar, A. G., and Mazzoleni, L. R.: Atmospheric organic matter in clouds: exact masses and molecular formula identification using ultrahigh-resolution FT-ICR mass spectrometry, Atmos. Chem. Phys., 13, 12343–12362, doi:10.5194/acp-13-12343-2013, 2013.

ACPD
14, 24753–24810, 2014

Table 1. Filters collected during the 2012 field campaign at the Pico Mountain Observatory. Only dry filters used for the laboratory analysis are included (Figure 1). Collection times for all filter samples are 24 h, except 6/29 (142 h) and 7/26 (52 h). Sampling times are given for local time (UTC). Average ambient concentrations of filter-collected $PM_{2.5}$ species are given, as well as the BC mass concentrations measured with the Aethalometer at 7-wavelengths averaged to the filters collection periods. All measurements are given with their respective standard deviations (1σ).

Filter name	Sampling start		Sampling end		Average flow	Measured ambient mass concentrations ($ng\,m^{-3}$)					
	Date (mm/dd/yy)	Time	Date (mm/dd/yy)	Time	($m^3\,h^{-1}$)	Org ± SD	EC ± SD	BC ± SD	SO_4^{2-} ± SD	NO_3^- ± SD	Cl^- ± SD
6/29	06/29/12	18:50	07/05/12	16:00	50	996 ± 5	58 ± 1	74 ± 8	1130 ± 8	24 ± 1	<DL
7/26	07/26/12	14:00	07/28/12	18:00	67	1038 ± 16	24 ± 5	33 ± 2	184 ± 30	50 ± 1	2 ± 9
9/1	09/01/12	18:00	09/02/12	17:55	84	195 ± 24	32 ± 13	32 ± 9	225 ± 16	270 ± 14	<DL
9/2	09/02/12	18:00	09/03/12	17:55	84	258 ± 10	34 ± 7	14 ± 1	134 ± 50	209 ± 15	<DL
9/3	09/03/12	18:00	09/04/12	17:55	81	124 ± 7	30 ± 4	8 ± 1	99 ± 39	210 ± 9	<DL
9/14	09/14/12	15:00	09/15/12	15:00	83	390 ± 29	0.7 ± 0.1	6 ± 1	29 ± 0	20 ± 0	18 ± 0
9/15	09/15/12	15:00	09/16/12	15:00	83	322 ± 29	1 ± 1	4 ± 1	40 ± 10	24 ± 12	30 ± 8
9/16	09/16/12	15:00	09/17/12	15:00	83	365 ± 17	1 ± 1	4 ± 1	47 ± 20	21 ± 1	18 ± 5
9/17	09/17/12	15:00	09/18/12	15:00	83	547 ± 15	1 ± 1	4 ± 1	42 ± 14	42 ± 34	8 ± 4
9/24	09/24/12	15:00	09/25/12	15:00	84	2049 ± 16	52 ± 1	62 ± 2	470 ± 14	248 ± 26	<DL
9/25	09/25/12	15:00	09/26/12	15:00	81	735 ± 46	20 ± 1	31 ± 5	75 ± 8	207 ± 11	17 ± 5
9/26	09/26/12	15:00	09/27/12	14:55	83	707 ± 86	18 ± 1	25 ± 2	289 ± 41	111 ± 13	105 ± 7
9/27	09/27/12	15:00	09/28/12	14:55	84	778 ± 1	18 ± 1	24 ± 1	266 ± 23	141 ± 2	<DL
9/28	09/28/12	15:00	09/29/12	14:55	81	293 ± 3	21 ± 2	13 ± 2	283 ± 5	192 ± 13	<DL
9/29	09/29/12	15:00	09/30/12	14:55	83	444 ± 1	16 ± 1	14 ± 1	208 ± 25	204 ± 19	<DL
9/30	09/30/12	15:00	10/01/12	14:55	83	160 ± 9	14 ± 1	5.0 ± 0.4	145 ± 15	167 ± 9	<DL
10/1	10/01/12	15:00	10/02/12	14:55	83	366 ± 6	0.3 ± 0.1	0.8 ± 0.1	36 ± 2	29 ± 18	39 ± 1
10/2	10/02/12	15:00	10/03/12	14:55	83	192 ± 1	1 ± 1	5 ± 1	46 ± 9	52 ± 2	42 ± 7

ACPD
14, 24753–24810, 2014

Table 2. Chemical characterization of the WSOC compounds detected in 9/24 and 9/25 samples. Averages of three replicate analyses (O/C, H/C, OM/OC, and DBE) with calculate standard deviation (1σ) of each data subset are given. Subscript "w" denotes values weighted by relative abundance (O/C_w, H/C_w, OM/OC_w, and DBE_w) which have propagated standard error computed using the standard deviations for each subset (Mazzoleni et al., 2010; Zhao et al., 2013).

		All	CHO	CHNO	CHOS
9/24	Number of molecular assignments	3960	2822	1124	14
	O/C	0.46 ± 0.13	0.47 ± 0.14	0.45 ± 0.10	0.50 ± 0.11
	O/C_w	0.47 ± 0.01	0.47 ± 0.01	0.46 ± 0.01	0.43 ± 0.27
	H/C	1.17 ± 0.26	1.19 ± 0.27	1.14 ± 0.22	1.75 ± 0.31
	H/C_w	1.17 ± 0.03	1.17 ± 0.03	1.14 ± 0.03	1.88 ± 1.01
	OM/OC	1.73 ± 0.18	1.72 ± 0.18	1.76 ± 0.15	1.99 ± 0.15
	OM/OC_w	1.73 ± 0.03	1.72 ± 0.03	1.77 ± 0.03	1.91 ± 0.70
	DBE	10.7 ± 4.0	10.8 ± 4.3	10.3 ± 2.9	3.5 ± 2.6
	DBE_w	10.2 ± 0.2	10.1 ± 0.2	10.6 ± 0.2	1.8 ± 1.5
	Number of molecular assignments with structure inferred by AI: Aliphatic (AI = 0)	2194	1686	494	14
	Olefinic (0.5 > AI > 0)	1563	1005	558	0
	Aromatic (AI ≧ 0.5)	203	131	72	0
9/25	Number of assigned formulas	4770	3272	1209	289
	O/C	0.42 ± 0.14	0.42 ± 0.15	0.42 ± 0.11	0.41 ± 0.15
	O/C_w	0.43 ± 0.01	0.43 ± 0.01	0.43 ± 0.01	0.35 ± 0.06
	H/C	1.28 ± 0.30	1.28 ± 0.30	1.18 ± 0.23	1.70 ± 0.27
	H/C_w	1.26 ± 0.04	1.26 ± 0.04	1.19 ± 0.03	1.73 ± 0.26
	OM/OC	1.67 ± 0.20	1.67 ± 0.20	1.72 ± 0.15	1.85 ± 0.21
	OM/OC_w	1.68 ± 0.03	1.66 ± 0.04	1.74 ± 0.03	1.79 ± 0.19
	DBE	9.4 ± 4.23	9.8 ± 4.4	9.8 ± 2.9	3.6 ± 2.3
	DBE_w	9.1 ± 0.2	9.2 ± 0.2	10.1 ± 0.2	3.2 ± 0.4
	Number of molecular assignments with structure inferred by AI: Aliphatic (AI = 0)	2740	1956	506	278
	Olefinic (0.5 > AI > 0)	1801	1169	622	10
	Aromatic (AI ≧ 0.5)	229	147	81	1

ACPD
14, 24753–24810, 2014

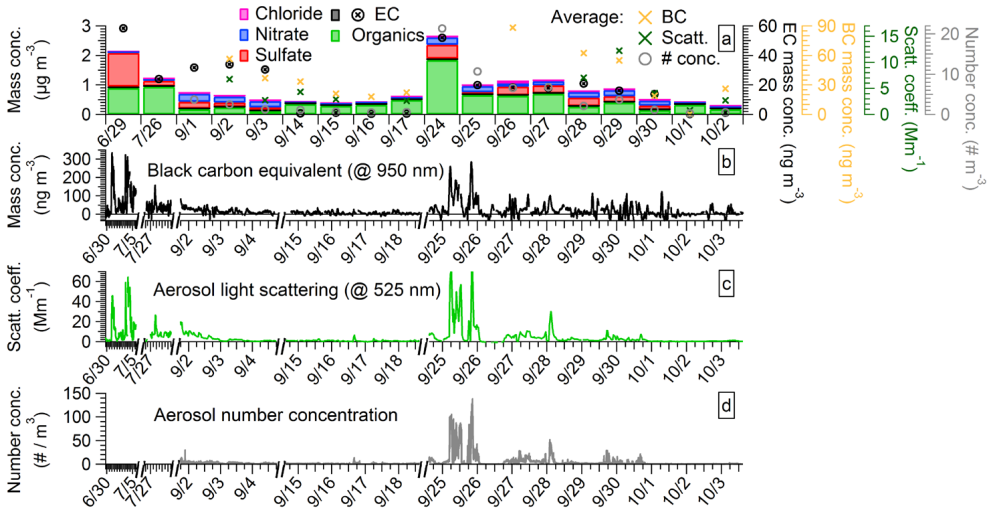

Figure 1. Time series of filter-collected aerosol during the 2012 field campaign **(a)**. The name of each filter measurement labeled on the x-axis is defined as the start date of measurement. Also shown are time series of the collocated black carbon **(b)**, aerosol light scattering **(c)** and particle number concentration **(d)** measurements for the periods overlapping with filter measurements. Note, on-line measurements are shown for the entire overlapping periods and thus each 24 h period in **(b–d)** might not perfectly overlap with the filter-collected periods in **(a)**. The on-line measurements of BC mass concentration, aerosol light scattering and number concentration were averaged for the sampling periods overlapping with filter measurements and are represented by symbols in **(a)**; these averages represent a simultaneous comparison with filter-collected species.

ACPD
14, 24753–24810, 2014

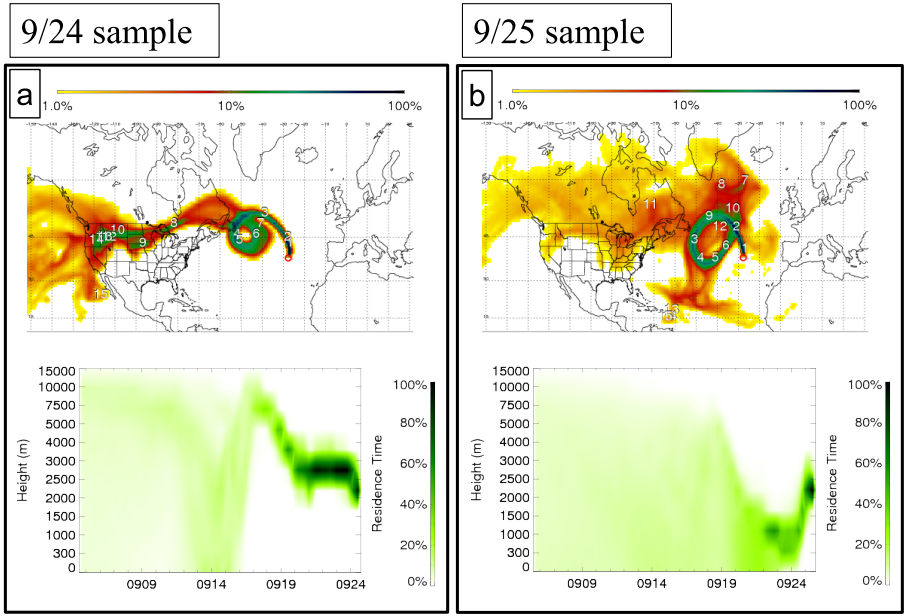

Figure 2. Examples of representative FLEXPART retroplumes for the 9/24 **(a)** and 9/25 **(b)** samples with locations at each upwind time labeled by white numbers in days. **(a)**: Retroplume simulation for 25 September 2012 at 6 a.m. for the peak values in BC on-line aerosol measurements. **(b)**: Retroplume simulation for 26 September 2012 at 6 a.m. for low values of on-line aerosol measurements (Fig. 1). Times are in UTC (local time). FLEXPART retroplumes for the entire period of the case study during which filter-collected aerosol were sampled are given in Supplement Figs. S4 and S5. Residence times of retroplumes are normalized by each vertical intervals in the lower plots to be able to better visualize the distribution along an irregular height scale.

ACPD
14, 24753–24810, 2014

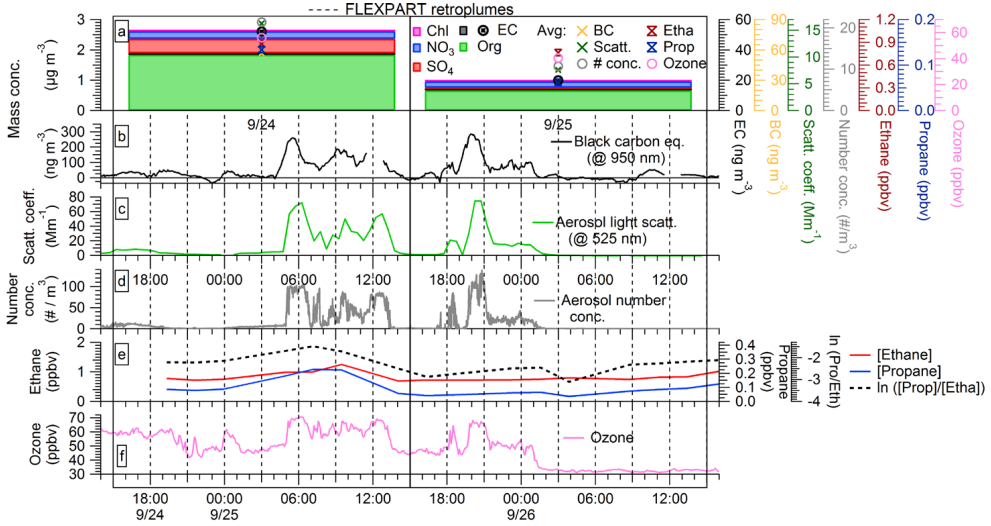

Figure 3. Comparison of aerosol measurements **(a–d)** during the 24–26 September case study with available gas-phase measurements of NMHCs ethane and propane **(e)** and ozone **(f)**. All on-line measurements are also given as averages during the sampling periods overlapping with filter measurements in **(a)**. Marked within the figure are the exact times of filter-collection periods (two black rectangular shapes, as given in Table 1) and FLEXPART retroplume simulations (dashed lines, as shown in Fig. 2 and Supplement Figs. S4 and S5). All continuous measurements in **(b–f)** have identical span of times and dates in *x* axis, times; times and dates are shown only in **(d)** and **(f)**.

ACPD
14, 24753–24810, 2014

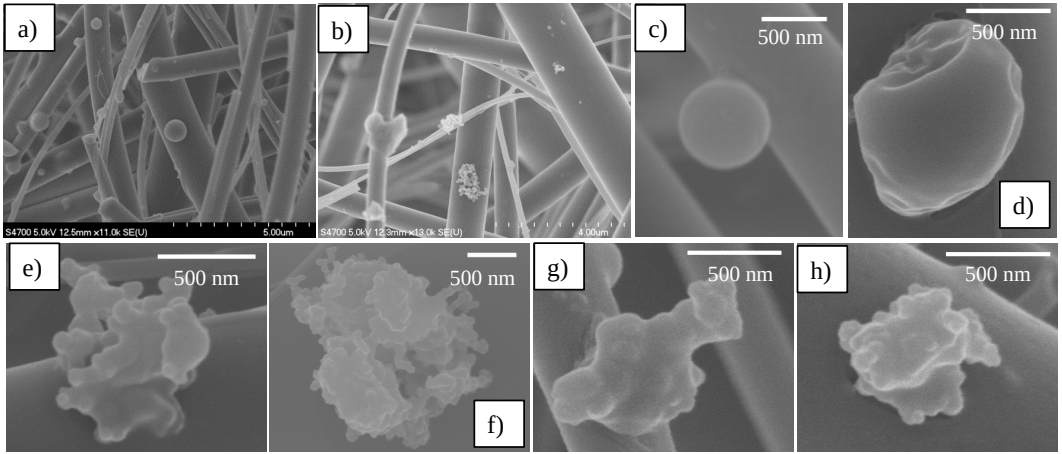

Figure 4. Representative SEM images of 9/24 **(a)** and 9/25 **(b)**. Also shown are examples of spherical **(c)** and near spherical particles **(d)**, as well as heavily coated soot particles from 9/24 **(e–h)**.

ACPD
14, 24753–24810, 2014

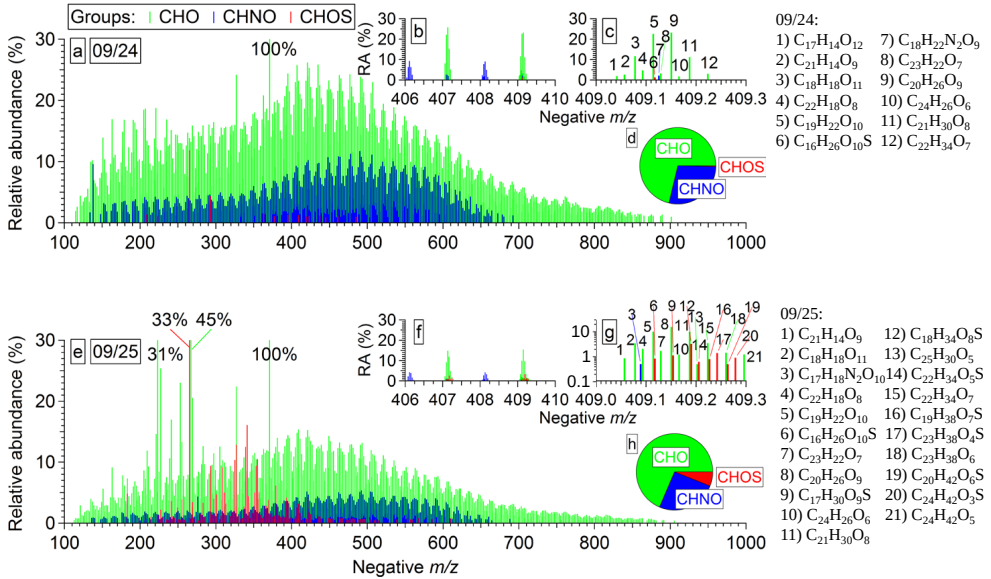

Figure 5. Reconstructed mass spectra of the assigned monoisotopic ions for PMO WSOC on 9/24 **(a–d)** and 9/25 **(e–h)** with CHO (green), CHNO (blue) and CHOS (red) groups of compounds. Number fractions of detected monoisotopic formula assignments in CHO, CHNO and CHOS compounds groups are given in the pie charts (**d** and **h**). An illustration of the isobaric complexity is shown as an excerpt of mass spectra between m/z 406–410 (**b** and **f**) and m/z 409.0–409.3 (**c** and **g**). All identified molecular formulas in both spectra between m/z 409.0–409.3 are listed in the order of appearance.

ACPD
14, 24753–24810, 2014

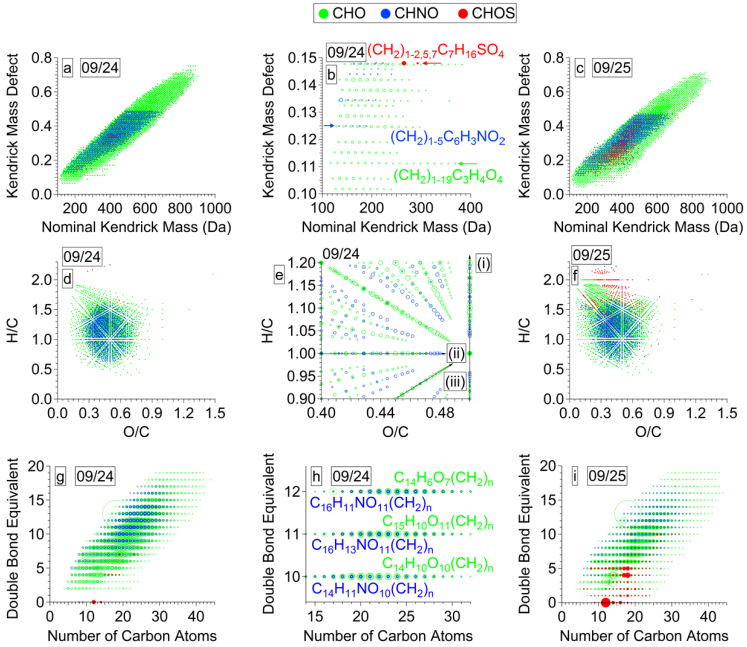

Figure 6. Top panels: Kendrick mass defect vs. nominal Kendrick mass for all of the monoisotopic molecular assignments in WSOC of 9/24 **(a–b)** and 9/25 **(c)**. Examples of homologous series of CHO, CHNO and CHOS groups of compounds are highlighted with arrows **(b)**. Middle panels: van Krevelen diagrams for all of the monoisotopic molecular assignments in WSOC of 9/24 **(d–e)** and 9/25 **(f)**. Examples of different chemical trends are highlighted with arrows and marked with letters (i), (ii) and (iii) **(e)**. Bottom panels: double bond equivalents vs. number of carbon atoms for all monoisotopic molecular assignments detected in WSOC 9/24 **(g–h)** and 9/25 **(i)**. Examples of CHO and CHNO species groups are given above and below, respectively, the DBE value **(h)**. The size of markers in **(b)**, **(e)** and **(g–i)** denotes relative abundance. **(b)**, **(e)** and **(h)** have magnified part of plot area to illustrate the chemical composition complexity available with FT-ICR MS analysis. See text for the details.

ACPD
14, 24753–24810, 2014

Molecular characterization of free tropospheric aerosol collected at the PMO

K. Dzepina et al.

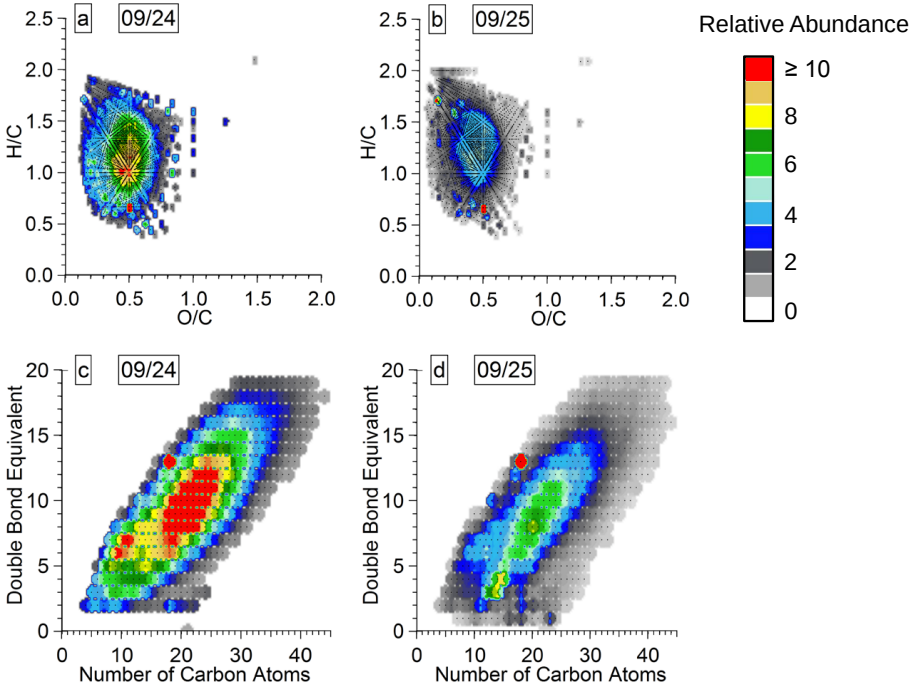

Figure 7. CHO isoabundance van Krevelen diagrams of 9/24 **(a)** and 9/25 **(b)** with all detected individual ions shown as dots to facilitate visualization of CH_2 homologous series. Also shown are the double bond equivalents vs. the number of carbon atoms of the 9/24 **(c)** and 9/25 **(d)** CHO group with symbol sizes representing the relative abundance.

ACPD
14, 24753–24810, 2014

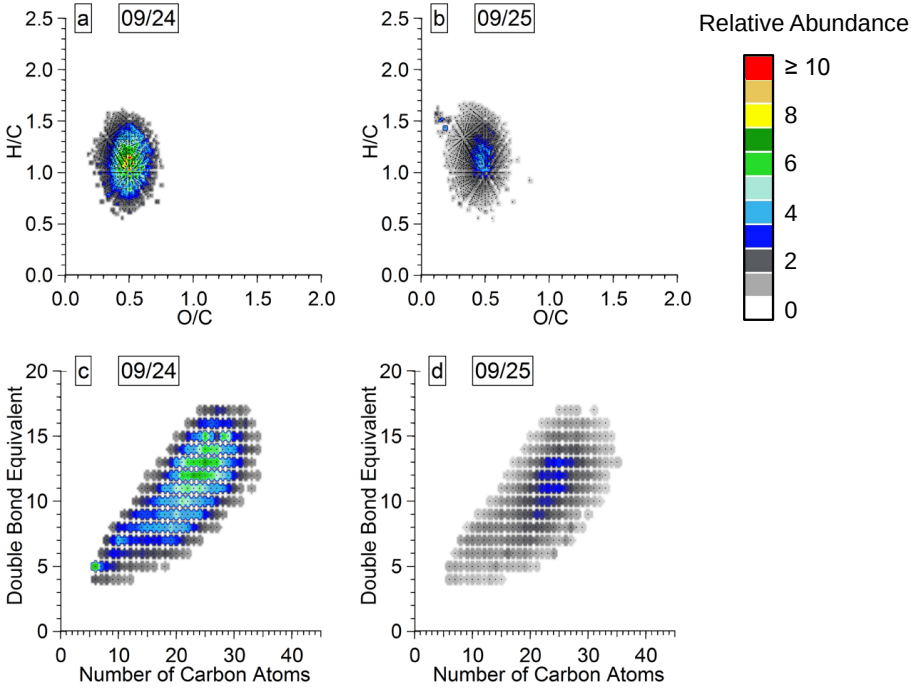

Figure 8. CHNO isoabundance van Krevelen diagrams of 9/24 **(a)** and 9/25 **(b)** with all detected individual ions shown as dots to facilitate visualization of CH_2 homologous series. Also shown are the double bond equivalents vs. the number of carbon atoms of the 9/24 **(c)** and 9/25 **(d)** CHNO group with symbol sizes representing the relative abundance.

ACPD
14, 24753–24810, 2014

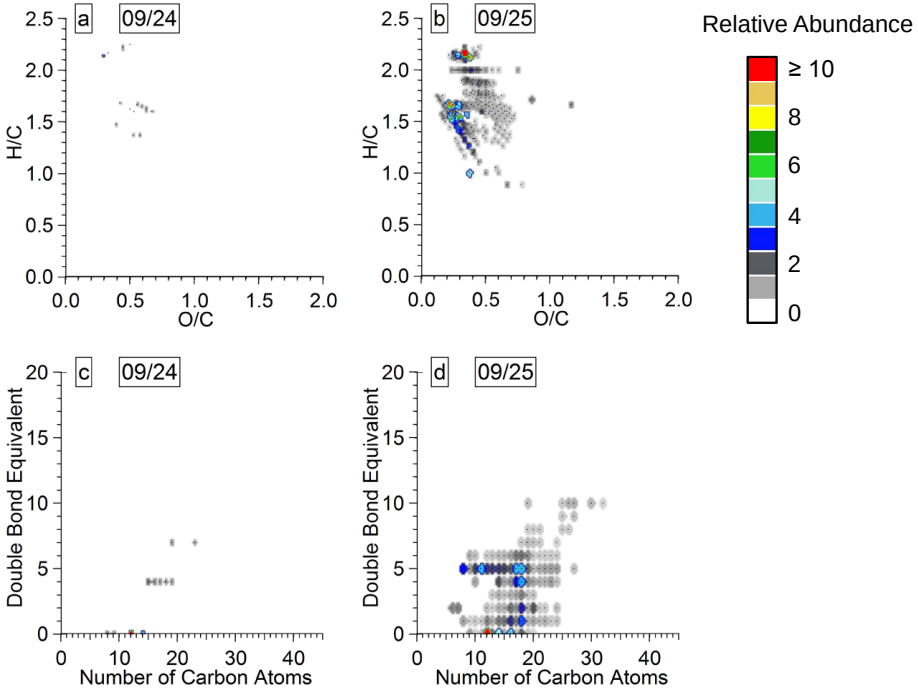

Figure 9. CHOS group species isoabundance van Krevelen diagram for 9/24 **(a)** and 9/25 **(b)** with all detected individual ions shown as dots to facilitate visualization of CH_2 homologous series. Also shown are the double bond equivalents vs. the number of carbon atoms of the 9/24 **(c)** and 9/25 **(d)** CHOS group with symbol sizes representing the relative abundance.

ACPD
14, 24753–24810, 2014

Figure 10

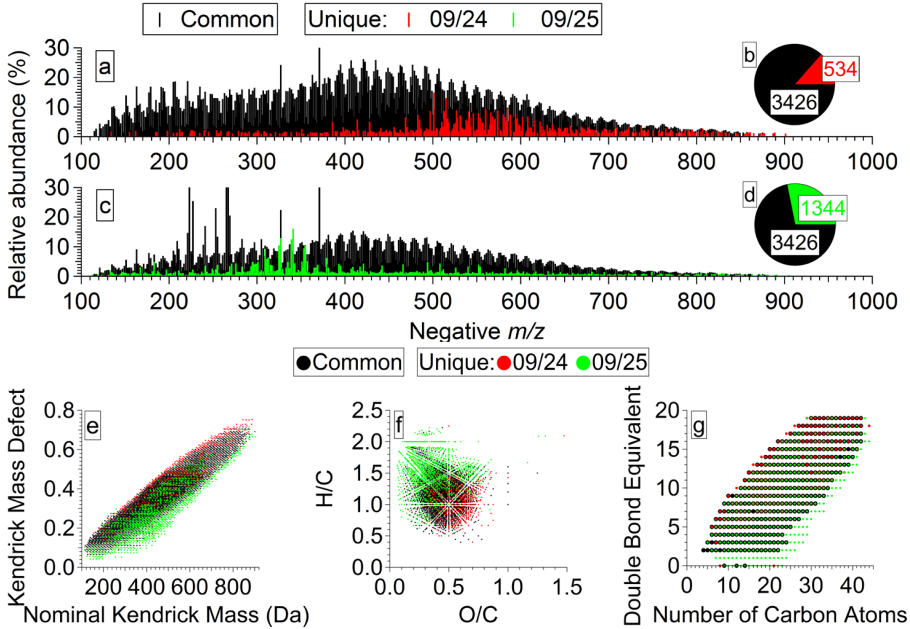

Figure 10. Mass spectra of 9/24 **(a)** and 9/25 **(c)** with common ions detected in both samples and ions unique for each sample. Pie charts indicate number fraction of common and unique molecular assignments detected in 9/24 **(b)** and 9/25 **(d)**; the exact numbers of common and unique assignment are given. Bottom panels: comparison of common and unique ions detected in PMO samples in Kendrick plot **(e)**, van Krevelen diagram **(f)** and double bond equivalents vs. the number of carbon atoms **(g)** figures.

ACPD
14, 24753–24810, 2014